TECHNISCHE UNIVERSITÄT DRESDEN

Operation of the X-Ray Detector at Felsenkeller Dresden and First Measurements

Bachelor-Arbeit
zur Erlangung des Hochschulgrades
Bachelor of Science
im Bachelor-Studiengang Physik

vorgelegt von

Christoph Seibt
geboren am 12.01.2001 in Pirna

Institut für Kern- und Teilchenphysik
Fakultät Physik
Bereich Mathematik und Naturwissenschaften
Technische Universität Dresden
2022

Summary

Abstract:

This thesis contains the installation of a low energy "SiriusSD® Silicon Drift Detector" as well as a background study and a first investigation on three samples, namely ^{151}Sm, ^{193}Pt and ^{158}Tb, which were recently activated with a neutron field at the DT generator of the IKTP at Helmholtz-Zentrum Dresden-Rossendorf. The experiment is built within the shallow-underground "Felsenkeller" laboratory, with 45 meter of rock overburden which massively reduces the rate of cosmic background radiation and is therefore used for low background setups. The measurements contain first test experiments to verify the settings followed by background measurements with two different detector orientations. Inspired by that the next experiment investigated the amount of muon induced signals in the detector. The next part was a first energy calibration and efficiency calibration, especially the energy calibration was necessary for the last experiments, namely the investigation of the new samples. These contain first spectra of the recently activated samples, which shall give a basic framework for further improvements and measurements done with these samples. The last part of this thesis contains a summary of the results, a discussion on how the experiments shall be improved and an outlook is given on the improvements and experiments that are important for the detector and the new samples.

Zusammenfassung:

Inhalt dieser Arbeit ist die Installation eines "SiriusSD® Silicon Drift Detector", sowie eine Untergrundanalyse und eine erste Untersuchung von drei Proben, namentlich ^{151}Sm, ^{193}Pt und ^{158}Tb, die mit einem Neutronenfeld am DT Generator des IKTP am Helmholtz-Zentrum Dresden-Rossendorf aktiviert wurden. Das Experiment wurde im "Felsenkeller" Untergrundlabor mit 45 Meter hohem Gesteinabdeckung aufgebaut, welches die Rate an kosmischer Strahlung massiv reduziert und dementsprechend für Experimente mit geringer Hintergrundstrahlung genutzt wird.

Die Messungen beinhalten erste Testexperimente zum Bestätigen der Einstellungen gefolgt von Messungen mit zwei verschiedenen Ausrichtungen des Detektors. Davon inspiriert untersucht das nächste Experiment die durch Myonen hervorgerufenen Signale. Im nächsten Abschnitt wurde eine erste Energiekalibrierung und Effizienzkalibrierung für den Detektor durchgeführt. Insbesondere die Energiekalibrierung war notwendig für das letzte Experiment, die Untersuchung neuer Proben. Diese enthält erste Spektren der kürzlich aktivierten Proben, was einen grundlegenden Rahmen für weitere Verbesserungen und Messungen mit den Proben liefern soll. Der letzte Abschnitt der Arbeit enthält eine Zusammenfassung der Ergebnisse, eine Disukssion bezüglich der Verbesserungsmöglichkeiten für die jeweiligen Experimente, sowie einen Ausblick auf wichtige Verbesserungen und Experimente für den Detektor und die neuen Proben.

Contents

1 Introduction

One of the most important parts of nuclear physics is the evaluation of radioactive samples to determine the properties of various nuclei as well as the properties of their decay. An efficient way to get information about the nucleus is to measure radiation emitted by the atom, which is usually done with a detector. Detectors therefore belong to the most important tools in nuclear and even particle physics, because they measure the radiation released during a decay process as well as the radiation coming from scattering processes. Nevertheless, before any kind of measurement can be done with the detector, the detector itself has to be characterized and its properties have to be determined.

Detectors exist in high numbers of varieties and are classified in various ways. Detectors can distinguish from each other depending on their detector material (e.g. ionization chambers, semiconductor detectors, ...), the measured particles (charged particles, neutrons, photons, ...) and the energy ranges for which they are sensitive. The detector investigated in this thesis is a "SiriusSD® Silicon Drift Detector" from "RaySpec Ltd". It is a low energy semiconductor detector mainly for photon detection, with an approximated energy range of a few keV up to 100 keV. This makes this detector a low energy detector, also called X-ray detector. X-rays are photons emitted by the atomic shell, but they also are emitted subsequently after the decay of a nucleus, so they can be used to characterize the decay of an unstable nucleus.

There are two major motivations behind this thesis. The first one is to build up a low energy low background photon detector in order to investigate nuclear structures and nuclear decay schemes. Low background detectors are highly important when events with a very low probability shall be measured, because the counting rate of such events is often smaller than the regular environmental background. There are lots of low background detectors, but almost no low energy low background detectors, so it is very interesting to have such a detector, especially in the investigation of radioactive samples with low activities (e.g. due to their low masses or long half-lives). The reduction of background radiation is done with shielding devices (e.g. lead blocks to reduce high energy background photons) or veto detectors (e.g. muon background), but before that the sources of background radiation have to be determined.

The second important motivation is the precise determination of half-lives of sources with negligible emission rates of γ-radiation. This is the case if e.g. the parent nucleus transfers directly to the ground state of the daughter nucleus during a decay process. In such a case the X-rays emitted by the daughter nucleus can be used to determine the half-life of the respective

decay.

The aim of this thesis is therefore to put a new X-ray detector into operation and to perform first experimental tests. A special focus lies on the characterization of the background sources, namely the impact of muon-induced events, intrinsic contaminations and the natural decay chains. The last part of this thesis includes measurements with three recently activated samples: ^{151}Sm, ^{193}Pt and ^{158}Tb. The purpose of these measurements is to investigate the photon spectra emitted by these sources in order to prepare and optimize later experiments on the determination of their half-lives.

The following chapter explains the theory behind photon radiation, their origin and interactions with matter as well as the shape of photon spectra and the physics of the used detector. Chapter three contains the detector setup and the radiation sources used during the measurements. This chapter is followed by the main part of the thesis, which contains the experiments and their subsequent analysis. It includes the results of the first experiments with the X-ray detector, as well as the importance of the detector orientation and the investigation of muon coincidence. After that, a fist detector calibration was done, including an energy and an efficiency calibration. The last part of the results is the investigation of the spectra of recently activated samples. The last chapter of this thesis is a summary and discussion of the results as well as an outlook containing the improvements and further experiments necessary before the detector can fully be used for its purpose.

2 Theory

Before one can start to write about experiments with a γ- and X-ray detector, a certain degree of general knowledge about radiation, detectors, data acquisition and its subsequent evaluation has to be established. The chapter is organized as it follows: In the beginning, relevant types of radiation are introduced, namely X-rays and γ-rays, followed by the decay types appearing in the experiments and the interactions of photons with matter. After these sections the shape and analysis of spectra is discussed, the detector physics are explained and the chapter is concluded with the detector calibration.

2.1 X-ray

X-ray is the name for electromagnetic radiation emitted during the transition of an atomic shell electron to a lower energy state. The atomic shell consists of orbits with different energy levels, labeled as K, L, M, etc. Every shell (except the K-shell) is also divided into a series of closely spaced subshells with individual energy levels. Depending on the configuration of the electrons, the atomic shell is in a certain energy state, with the lowest energy state being the ground state. Electrons are Fermi-particles, which means every shell can only contain a certain number of electrons (figure 2.1).

As common in nature, the atomic shell always wants to have the lowest energy level possible. If an atom is in an excited state, it will deexcite to the ground state. The energy loss due to the deexcitation can be dispensed via the emission of a photon, which is called X-ray. An atom is in an excited state, when at least one of the shells has a vacancy or hole, which could be filled by an electron from a higher energy level. If the excitation involves more than one shell, the deexcitation is usually done by a series of transitions, each can involve the emission of an X-ray. It is important to note that there are so called "hindered" transitions between energy levels with a low probability to appear due to quantum-mechanical rules. Possible X-ray transitions are shown in figure 2.2.

An alternative deexcitation process is the Auger effect, which has a small probability of appearing instead of X-ray emisson. In the Auger effect, the deexcitation energy is transfered to a weakly bound electron, which gets ejected from the atom as Auger electron. This process is less important for X-ray detectors due to the low range of electrons in matter, but it can occur as radiative Auger effect, where an Auger electron as well as an X-ray is created. This
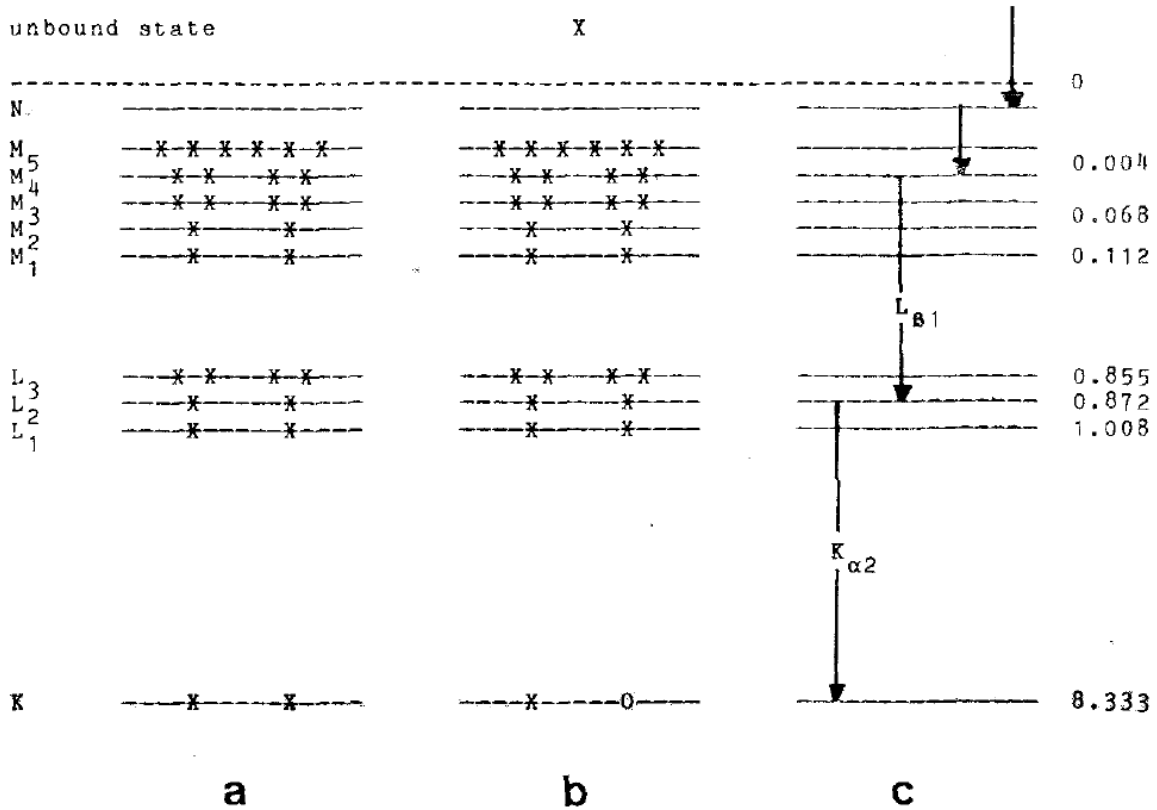
Figure 2.1: Electron configuration for a Ni atom: (a) ground state; (b) excitation of a K electron; (c) possible sequence of deexcitations.[3]

can cause a satellite peak on the low energy side of the X-ray peak. Every energy shell has a finite range of energies, with a mean energy E_0 and a full width at half maximum (FWHM) Γ. The energy distribution is given by the Lorentzian function

$$L(E) = \frac{\Gamma/2\pi}{(E - E_0)^2 + (\Gamma/2)^2}. \tag{2.1}$$

The width of an X-ray line can be obtained with the convolution of the Lorentzian functions of the included energy levels. The width of the X-ray line is given by the Γ of both levels:

$$w_{line} = \Gamma_{initial} + \Gamma_{final} \tag{2.2}$$

This width can sometimes be concerning in X-ray spectrometry. One last thing to say is that X-ray lines only depend on the atomic shell and not on the nucleus, which means the X-rays of any element do not depend on the isotope. [3]
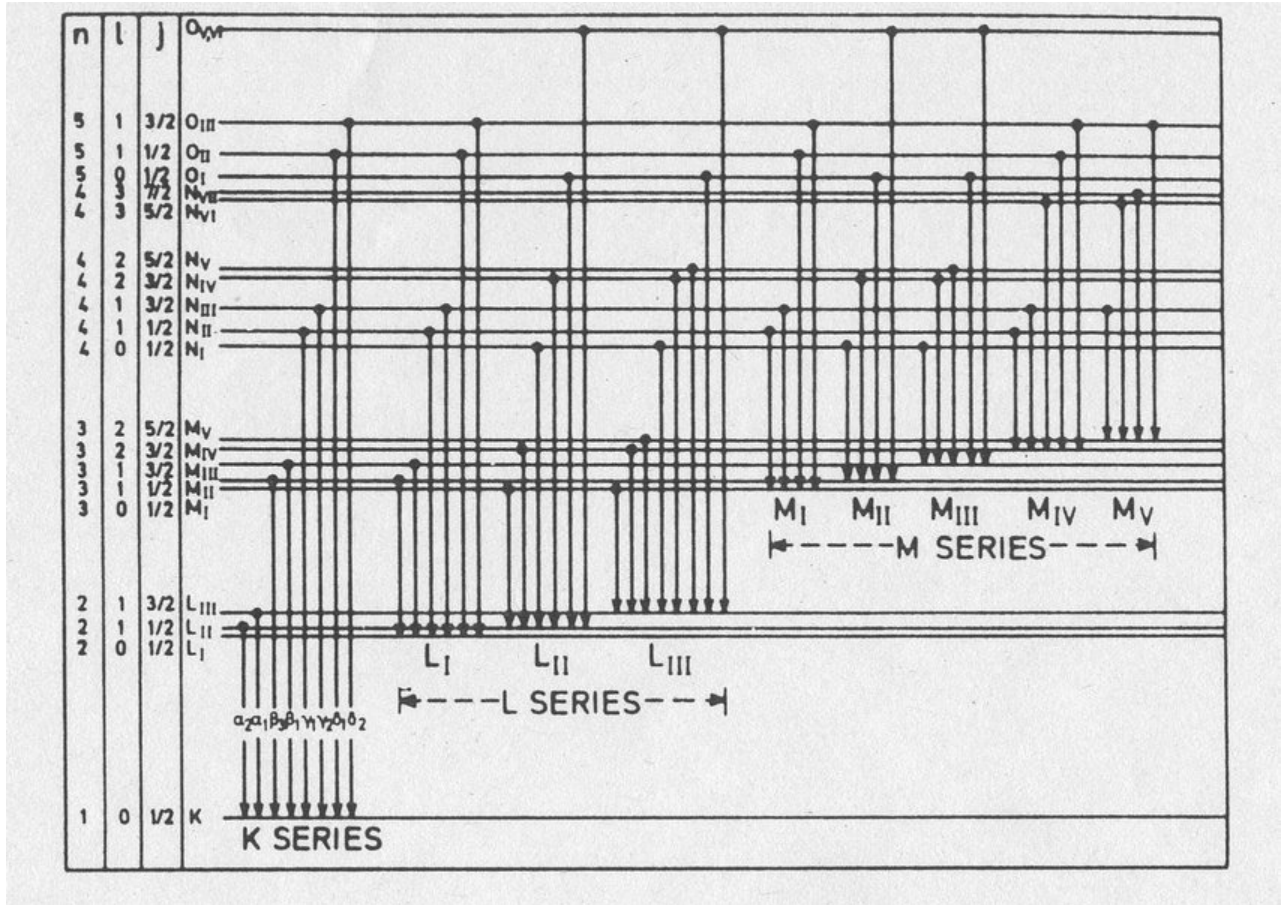
Figure 2.2: Nomenclature for different possible X-ray decays.[15]

2.2 γ-radiation

In analogy to the excited states of the atomic shell, the nucleus of an atom can also be excited. In order to reach the ground state, the nucleus can deexcite by the emission of a γ-ray photon. Excited states of a nucleus are usually obtained during decays such as α- or β-decays or electron-capture (EC), figure 2.3 shows an example for EC. In many cases the energy release of such a decay process is not entirely transferred to the emitted particles. Some amount of the energy is stored within the daughter nucleus, transmitting it in an excited state. This excited state then emits energy to reach the ground state by either emitting a γ-ray photon or by internal conversion.

The energy of a nuclear state is well-defined, which means the deexcitation energy is also discrete. Since the γ-ray emission from the nucleus can be considered as a two body problem, the momentum of the emitted photon is the exact opposite of the momentum of the nucleus due to momentum conservation. With energy conservation and the energies of the two nuclear states the energy of the γ-ray is calculated with

$$E_\gamma = E_i - E_f - E_R. \tag{2.3}$$
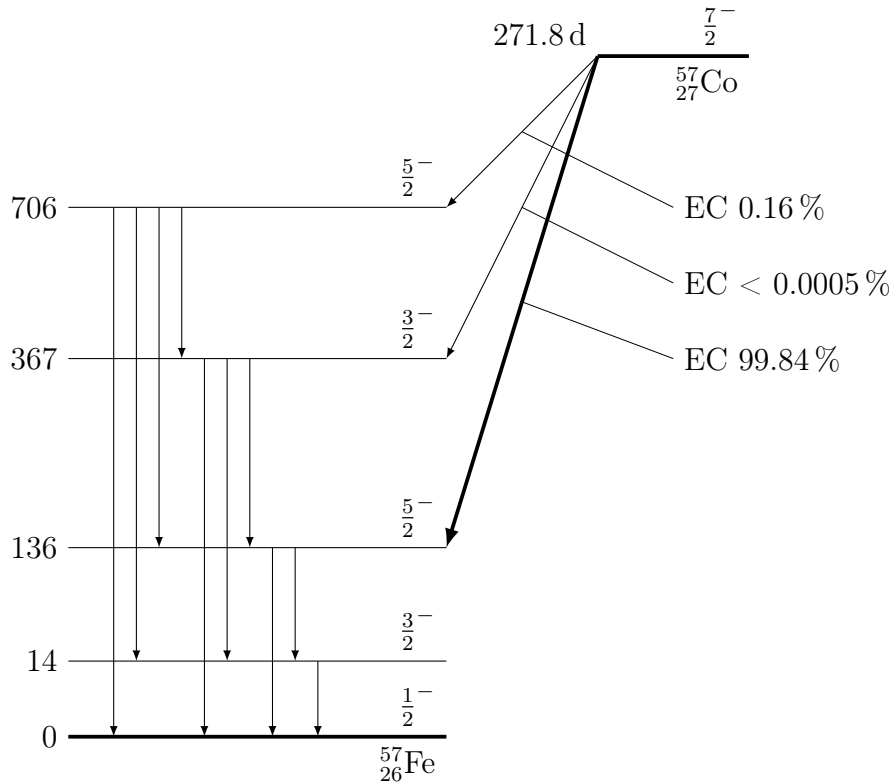
Figure 2.3: Decay scheme of ^{57}Co. The ^{57}Fe nucleus is in an excited state after the decay of ^{57}Co and deexcites via γ-emission.[3]

E_i and E_f are the energies of the initial and final states of the nucleus and E_R compiles to the recoil energy of the nucleus. There are several properties of the involved energy levels which are relevant in order to formulate selection rules for γ-transitions. Each energy level of a nucleus has a discrete total angular momentum $\boldsymbol{J}$ and parity π, which can either be positive $(+)$ or negative $(-)$. During the transition of a nucleus from an excited energy level to a lower energy level, the difference in parity and angular momentum has to be carried away by the γ-ray:

$$\boldsymbol{J}_i = \boldsymbol{J}_f + \boldsymbol{J}_\gamma, \tag{2.4}$$

$$\pi_i = \pi_f - \pi_\gamma. \tag{2.5}$$

The indices refer to the initial (i) or the final state (f) of the nucleus or to the properties of the γ-ray. The γ-ray always has at least one unit of angular momentum, so no γ-ray transitions with no change of angular momentum can occur. Depending on the angular momentum and the parity of the γ-ray each generated γ-ray can also be described with a certain multipolarity, which is EL (electric) or ML (magnetic), whereby L describes the order ($L = 1, 2, 3, \ldots$

corresponds to dipole, quadrupole, octupole, ...) and E1, M2, E3 etc. occur with a change of parity and M1, E2, M3 etc. without parity changes. The probability of a transition γ_i is higher the lower the multipolarity is, whereby the half-life of a nuclear state is inverse proportional to the transition probability.

The last point of this section is the internal conversion, which rivals the γ-decay. The energy difference between the nuclear states is transferred to an electron in the atomic shell, ejecting it from the atom. Since γ-decay and internal conversion can occur for a transition, the respective transition probability is equal to the sum of both transition probabilities, which is important to consider if one wants to determine the half-life of a transition.[3][11]

2.3 β^+-, β^--decay and electron capture

The previous chapters introduced the emitted radiation during the deexcitation of the atomic shell and atomic nuclei. For the scope of this thesis, the dominant reason for these emissions are preceded β^+, β^- and Electron captures (EC), which leave the nucleus or the shell in an excited state. These three decays are part of the weak interaction. They occur when the parental nuclide can decrease its mass by changing a proton into a neutron or vice versa. The number of nucleons as well as the number of leptons has to be conserved during each process. During the β^--decay, a neutron converts into a proton by emitting an electron, which is often referred to as β^--radiation.

$$n \rightarrow p + e^- + \overline{\nu_e} \tag{2.6}$$

The β^+-decay converts a proton into a neutron by emitting a positron, described as β^+-radiation.

$$p \rightarrow n + e^+ + \nu_e \tag{2.7}$$

Due to the creation of a positron, this decay is only possible if the mass difference between parental and daughter nuclide is higher than $2m_0$ (m_0 is the electron mass). The decay rivaling the β^+-decay is electron capture. This occurs when the wave functions of nucleus and shell electrons overlap. An electron can then be captured by a proton in the nucleus, which subsequently converts to a neutron.

$$p + e^- \rightarrow n + \nu_e \tag{2.8}$$

If the mass difference between parental and daughter nucleus are smaller than $2m_0$, then only EC can occur. Else, EC as well as β^+-decay can occur, but it strongly depends on the atomic wave functions and the mass difference which process is supressed and which dominates. For

some nuclei with even mass numbers it is also possible that they decay via β^--decay, β^+-decay and EC, due to the pairing energy of even proton and neutron numbers.[11]

2.4 Interactions of photons with matter

The interactions between photons and matter are obviously very important for γ- or X-ray detectors. On the one hand, these interactions are necessary for the detector to work, on the other hand they influence the spectrum taken of any source. The three main interactions are the photoelectric effect, the Compton effect and pair production. The detector used in the experiments is an X-ray detector, which detects particles with energies below 100 keV. Since pair production involves photons with more than 1022 keV, this effect is not relevant for our experiments. There are also other scattering processes, e.g. Rayleigh and Thomson scattering, which do not change the energy of the photon but the direction. And it is also possible for photons to interact with a nucleus. But these effects are by far less probable and less important for our experiments than the first two effects.

Photoelectric effect

The photoelectric effect describes the absorption of a photon within a bound electron of an atom. During the absorption of a photon its entire energy is transferred to the electron, which then leaves the atomic shell if the photon energy E_γ exceeds the binding energy E_b. The difference remains as kinetic energy E_e

$$E_e = E_\gamma - E_b \tag{2.9}$$

of the electron. The ejected electron loses its energy in the surrounding matter by secondary ionization processes along the trajectory. The photoelectric effect creates a hole in the atomic shell, which is filled by another electron from an outer shell. During this process X-rays and Auger-electrons are generated (chapter 2.1). These secondary particles are also absorbed, so that the total energy of the initial photon is transferred to the matter. This effect has the highest cross-section for low energy photons in comparison to other photon-matter-interactions.

Compton effect

The Compton effect describes the inelastic scattering of a photon with a weakly bound electron. The photon loses a part of its energy in this process which is transferred to the electron. The dependency between the scattering angle θ, the final photon energy E' and the electron energy E_e is given to

$$E' = \frac{E}{1 + \alpha(1 - \cos\theta)} \tag{2.10}$$

$$E_e = E \left[1 - \frac{1}{1 + \alpha(1 - \cos\theta)} \right] \tag{2.11}$$

with the initial energy of the photon E and $\alpha = E/m_0c^2$. The energy given to the photon increases with increasing scattering angle, that means a Compton-scattered photon has a minimal energy of $E' = E/(1 + 2\alpha)$ at 180° scattering angle.

Depending on the remaining energy, the scattered photon has the potential to scatter multiple times with Compton scattering before it gets absorbed with photoelectric effect. The initial photon leaves its energy in a bigger volume compared to photoelectric absorption.

The cross section of Compton scattering is higher at higher energies, so it is more dominant at high energies than the photoelectric effect. Figure 2.4 shows which effect is dominant for which atomic numbers and photon energies.[3]
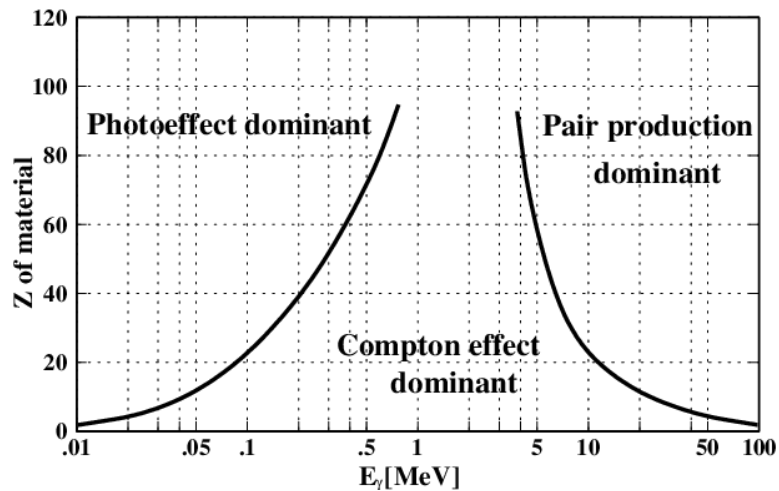

Figure 2.4: Dominant effect of three main photon-matter-interactions depending on photon energy and atomic number.[10]

2.5 Shape of spectra and peaks

2.5.1 Shape of spectra

The shape of a γ and X-ray spectrum usually includes the γ and X-ray lines of the investigated source as well as their spectral background. The definition of background in spectra analysis is a bit decisive, as it does not mean the spectrum without any source (environmental background). The background is actually every part of the spectrum except for the γ and X-ray line of interest. As shown in figure 2.5, a typical high energy spectrum consists of the full energy peaks of γ-rays, the environmental background and various effects due to the interactions between photons and matter. Many effects in high energy spectra occur due to pair produc-
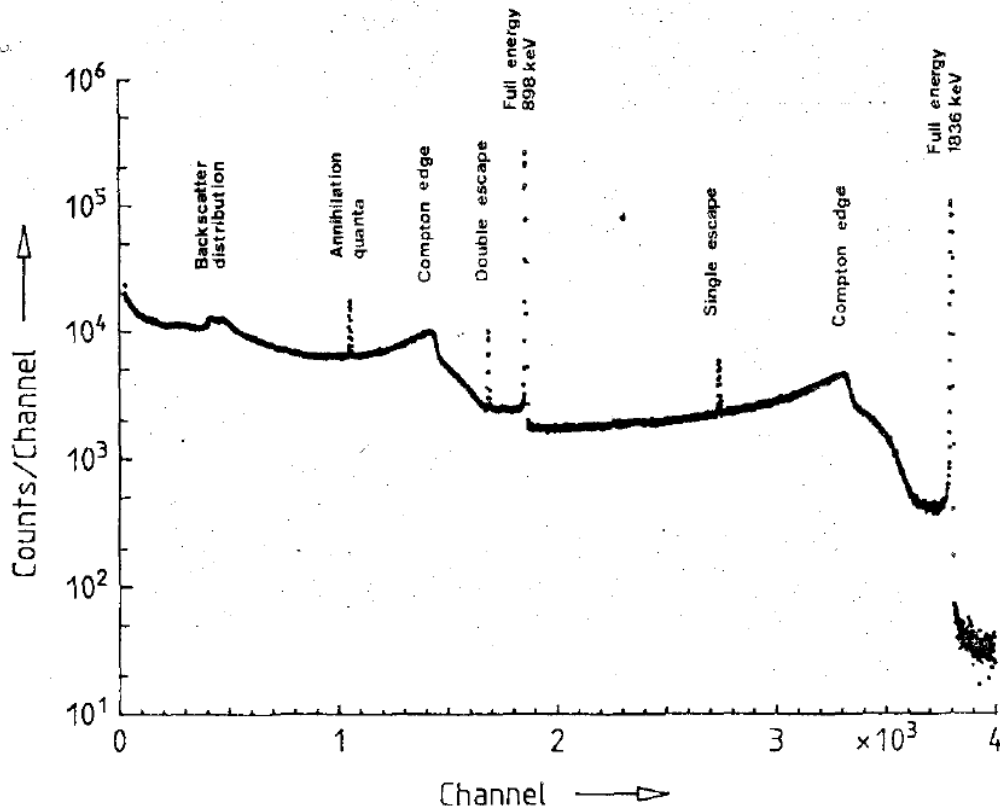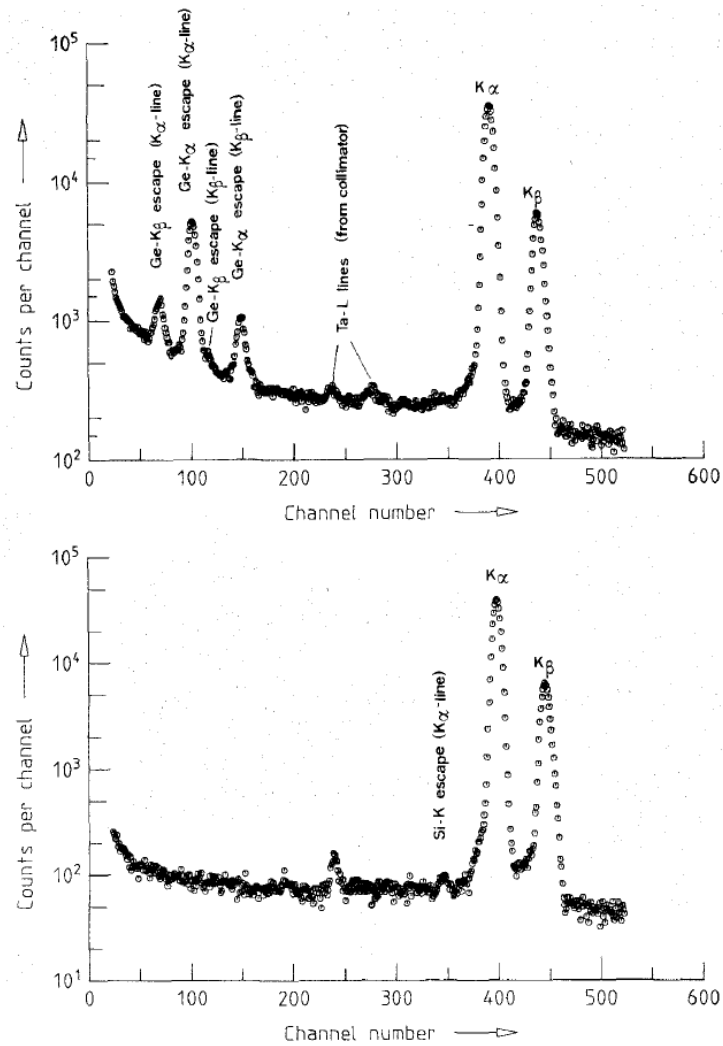
Figure 2.5: Pulse-height spectrum of a ^{88}Y source, Ge(Li)-detector.[3]

tion, these are the single escape peak, the double escape peak and the annihilation quanta peak. As said previously, low energy γ- and X-ray photons have too little energy for pair production to occur. The first effect to cover that is interesting for low energy photons is the Compton-effect, which, as mentioned earlier, creates a free electron with an energy between 0 and $E/(1 + m_0 c^2/2E)$, and a scattered photon with an energy between $E/(1 + 2E/m_0 c^2)$ and E. If this happens within the detector, two things could happen. The scattered photon can interact with the detector crystal, which means the full energy of the initial photon contributes to the event and the event is part of the full energy peak. The scattered photon can also escape, which means the event only contains the electron energy. The maximum electron energy marks the Compton edge. If the Compton effect takes place in the material behind the detector, the scattered photon can be recorded by the detector, which leads to the backscatter distribution.

The second important interaction is the photoelectric effect, which contributes to the full energy peak, with some conditions:

During the photoelectric effect energy is lost due to the binding energy of the photoelectron. This creates secondary X-rays, which have to lose their energy in the detector, or else leading to X-ray escape peaks. These peaks are especially shown in figure 2.6. This shows that the X-ray escape peaks are more dominant in Ge-detectors and less dominant in Si(Li)-detectors. The second condition is that the full energy of the photoelectron has to contribute to the event.

Figure 2.6: Pulse-height spectrum of X-rays of a [85]Sr source, Ge-detector (top) and Si(Li)-detector (bottom).[3]

The escape of Bremsstrahlung and photoelectrons leads to entries below the full energy peaks. It is also important that trapping effects and charge-collection losses don't have an important influence during the measurements, as they would lead to a tailing on the low energy peak side.

2.5.2 Shape of peak and background

It is useful to describe a peak with two functions, one for the background in the peak and one for the peak itself. As said previously, the background should describe everything in the peak area except for the actual peak, which includes tailing from other peaks next to the interesting peak as well as the effects discussed previously.

The first thing to note for the background is that the background on the low energy side of the peak is stepwise higher than the background on the high energy side. Reason for that is that the photon or through interaction "produced" electrons have various ways to lose small

amounts of energy. There are lots of functions created to approximate the background, going from a constant function to a third-order polynomial to even more complex functions like the Gaussian error function.

A simple function to describe the background of a single peak for low energy measurements is a linear function. The first aspect that makes this function useful is that it is easy to calculate and handle. If a spectrum has one single peak or a few peaks close together, one can simply take intervals on both sides of the peak(s) and calculate the background function with these points. The second aspect is that the background is usually much smaller than the peak itself, which allows the background function to be a bit less sufficient.

The second function for the peak description is the function for the peak itself. If tailing is not assumed, the most accurate function describing the peak of a γ-ray line is the Gaussian function

$$G(x) = Y \cdot \mathrm{e}^{\frac{-(x-\mu)^2}{2\sigma^2}} \tag{2.12}$$

with the amplitude Y, the centroid μ and the standard derivation σ, which is related to the FWHM w with $w = 2.35 \cdot \sigma$. An alternative expression of the Gaussian function is

$$G(x) = \frac{N}{w\sqrt{\pi/4 \cdot \ln 2}} \cdot \mathrm{e}^{\frac{-(x-\mu)^2}{2\sigma^2}} \tag{2.13}$$

with the peak area N. The Gaussian function is used to describe peaks with a small amount of tailing on both sides, which ideally is the form of a γ-peak. The reason for the Gaussian function is that the energy measured during an event follows the Gaussian distribution. But sometimes the measured peak has small deviations from the respective Gaussian function. To cancel out such deviations, additional terms can be added to the Gaussian function. These terms are often used to describe the tailing on both sides of the peak. However, it always depends on the analyzed spectrum and the purpose of the analysis how accurately the peak has to be described. Also due to the development of detector technology modern detectors produce less tailing, which decreases the impact tailing functions have on spectrum analysis. It is also worth mentioning that the amount of fitted parameters increases, which leads to more covariances between the fitting parameters. In practical spectrum analysis when tailing is included, the parameters that describe the tailing are described as dependent on the energy of the γ-ray line.

Up until now only the shape of γ-peaks have been discussed, without mentioning X-ray peaks. As mentioned previously, the shape of an X-ray line is described with the Lorentzian function

$$L(E) = \frac{\Gamma/2\pi}{(E - E_0)^2 + (\Gamma/2)^2}, \tag{2.14}$$

with the energy E, the energy of the line E_0 and the line width Γ. This function has a larger tailing than the Gaussian function. Since the energies measured by a detector follow the Gaussian distribution, the function representing the measured peak of an X-ray line is a convolution of Lorentzian and Gaussian function, the Voigt function:

$$V(E) = \int_{-\infty}^{+\infty} L(E') \cdot G(E - E') \mathrm{d}E \tag{2.15}$$

As shown in figure 2.7 the Gaussian function is the dominant part of the convolution for a
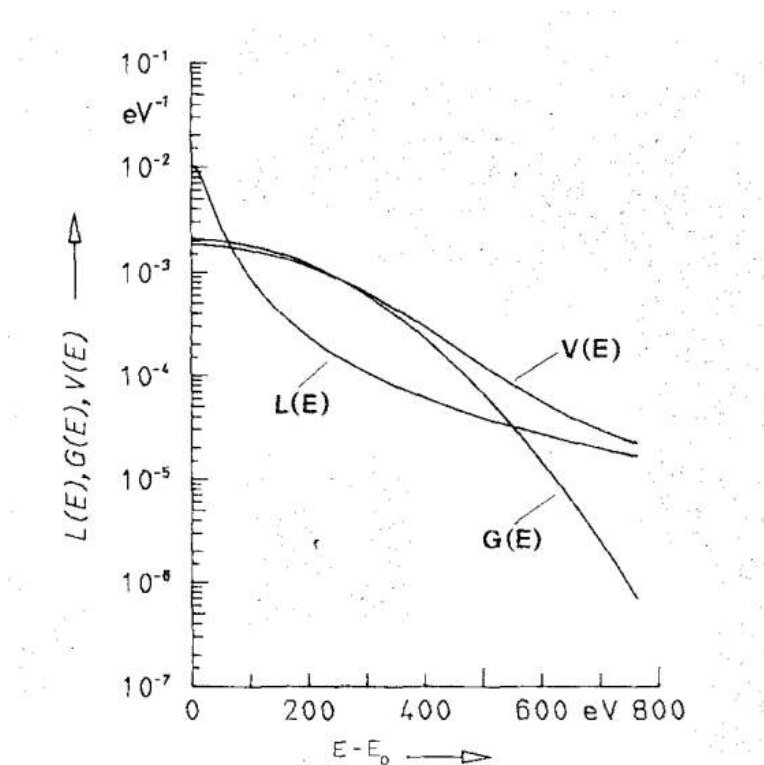
Figure 2.7: Halfes of a Lorentzian function $L(E)$ with $\Gamma = 62$ eV, a Gaussian function $G(E)$ with $w = 450\,$eV and their convolution, the Voigt function $V(E)$, for $E_0 = 75\,$keV. The functions are normalized.[2]

majority of the peak. The Lorentzian function influences the tailing a lot, which influences the area distribution of the investigated line. However, a major problem of the Voigt function is that it is difficult to fit because it is not an analytical expression. This makes it necessary to either find approximating analytical expressions or use a numeric method to fit the function, which could be difficult to realize. Depending on the evaluation methods used, a Gaussian function can be sufficient to describe the peak of an X-ray line.

If peaks are highly influenced by other peaks, meaning that the peak width and the distance between the peaks have the same order of magnitude, it is necessary to add functions describing the other peaks to the function describing the peak of interest.

2.6 Peak evaluation

The most important reason to measure and evaluate spectra is to find the emission rates of photons for a specific energy. This means the number of entries in a peak has to be determined. There are various methods to determine the peak area, but the determined areas for a peak will usually distinguish due to the definition of which entries belong to the peak area and how it is determined. For a good evaluation method it is more important to be reproducible than to cover the peak area as accurately as possible. A method might not cover the complete area of a peak, but when this method is used for both the efficiency calibration and the evaluation of investigated peaks, the potential deviations cancel out.

The simplest method to determine the peak area is the summation method, where the entries in the peak are added up. The major questions of this method are how many channels are used for the summation and how to define the respective background. For the first question, one solution is to fit the peak with a Gaussian function, which gives the peak position μ, the FWHM w and the Gaussian peak N_g, which can be compared to the peak area N_s determined by summation. The range of channels used for summation is chosen typically between $2 \cdot w$ and $3 \cdot w$ around the centroid, with $2.55 \cdot w$ taking 99.7% into account. It is important to only partially include the channels at the edges of the determined range. The background is determined with a range of channels on both sides of the peak ($N_{b,l}$ and $N_{b,r}$), each range as big as $1/2$ of the peak range. The difference between peak area and background is the actual peak area: $N = N_s - N_b$, with an uncertainty of $\sqrt{N_s + N_b}$. This method is illustrated in figure 2.8 There are also even simpler methods used, one could for example define a range of
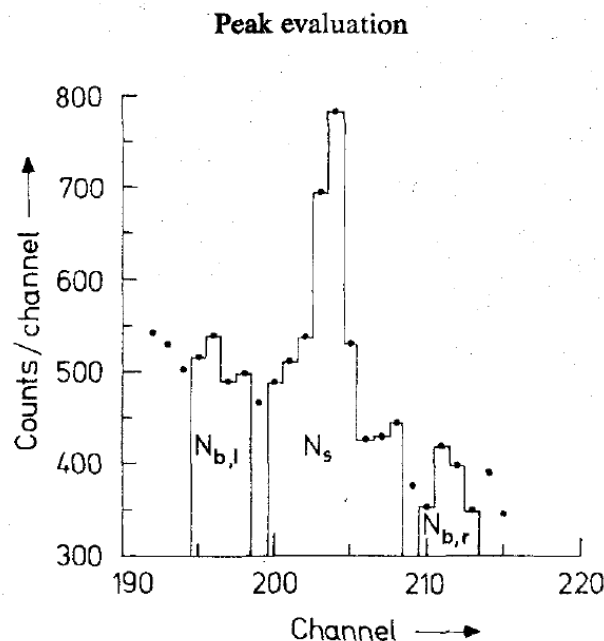

Figure 2.8: Simplified explanation of the summation method.[3]

channels for the peak location and add them up, with the first and last channel of this range defining the background. But due to choosing the range depending on the peak this method is probably less reproducible.

An analytic method is to determine the exact function describing the peak, which includes the peak function (Gaussian), possible tailing, a background function and possible secondary peaks within the main peak area. The peak area can then be gathered by integrating over the functions that describe the entries produced by the investigated γ or X-ray line. If only a Gaussian function describes the peak, the peak area is

$$N = Y \cdot w \cdot \sqrt{\frac{\pi}{(4 \cdot \ln 2)}}. \tag{2.16}$$

If there are functions describing the tailing of the peak, it has to be discussed which functions can be accorded to the peak and which functions are defined as part of the background. In this thesis peaks are fitted with normalized Gaussian functions (2.13). The fitted area of the Gaussian function corresponds to the peak content of the analyzed peak. The background is fitted as a constant function, while secondary peaks are described with respective Gaussian functions.
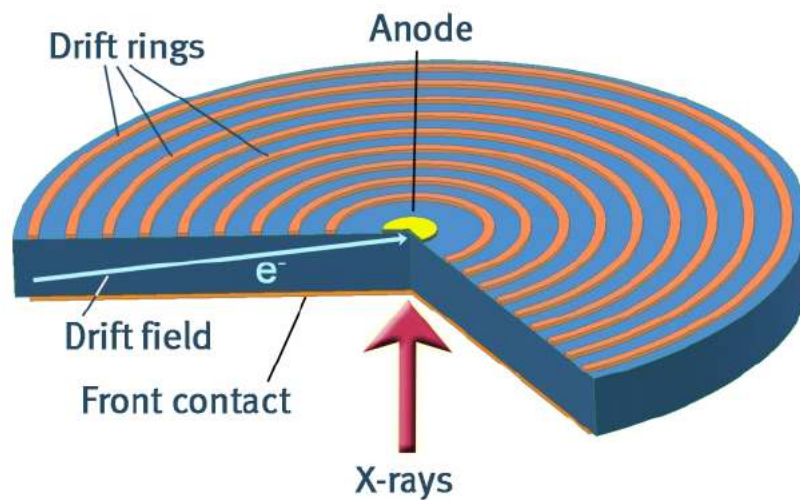
2.7 Silicon drift detectors

This section shall give an introduction to semiconductor detectors (e.g. silicon detectors), their working principle, and also to so called silicon drift detectors (SDD), which are used for the following experiments. The basis of a silicon drift detector is silicon, a semiconductor with four valence electrons, where the atomic shells are connected to almost continoous bands, with forbidden spaces between them. In a semiconductor, the highest band (valence band) is completely filled in the ground state. The energy necessary to lift electrons in the next higher band (conduction band) is very low (3 eV for silicon), which makes it easy to excite electrons into the conduction band. When electrons in a semiconductor are lifted in the conduction band, a hole is created in the valence band. Both together (the so-called electron-hole-pair) act as free charge carriers within the semiconductor. It is possible to bring electrons and holes into a semiconductor by "doping" them with atoms with more (n-type) or less (p-type) than four valence electrons. These atoms remain as positive (n-type) or negative (p-type) ions which creates forward and reverse bias direction.

When a photon enters the detector, it ionizes the matter creating free electrons. These electrons are slowed down, exciting electrons and creating electron hole pairs, which can move freely across the semiconductor. By applying an electric field, the electrons and holes can move to the anode and cathode inducting a current pulse.

A silicon drift detector, as shown in 2.9, consists of n-type silicon and p-type front contact and

drift rings. On these two, a negative bias voltage is applied, which fully depletes the silicon. The negative potential increases from the ring closest to the anode to the outest ring, which creates a drift field to guide electrons to the anode. When photons interact with the silicon, electron-hole-pairs are created and the electrons move to the anode and create a change of current. The integral over the change of current, which is the charge produced by the photon, is the strength of the signal and directly correlated to the photon energy. The holes are collected by the p-type regions. The used detector has thermoelectric coolers, which leads to a working temperature of a few tens below $0\,°C$. This still comparatively large temperature leads to thermally induced electron-hole-pairsand thus to a leakage current, which is integrated over a certain time until a reset pulse is applied. In contrast to the smooth baseline of a HPGe detector, SDD's therefore show a sawtooth-like baseline as shown in figure A.1. [6][8][12]


**Figure 2.9:** Schematic sturcture of a silicon drift detector.[12]

3 Experimental setup

3.1 Setup and acquisition software

Before the setup itself is introduced, it is important to mention the location of the setup, the "Felsenkeller" laboratory owned by the "Helmholtz Zentrum Dresden Rossendorf" in collaboration with the institute for nuclear and particle physics in Dresden. The laboratory is part of a tunnel system created in 1856-1859, the height difference between tunnel and surface is up to 45 m high. The tunnel system is shown in figure 3.1. The rock surrounding the
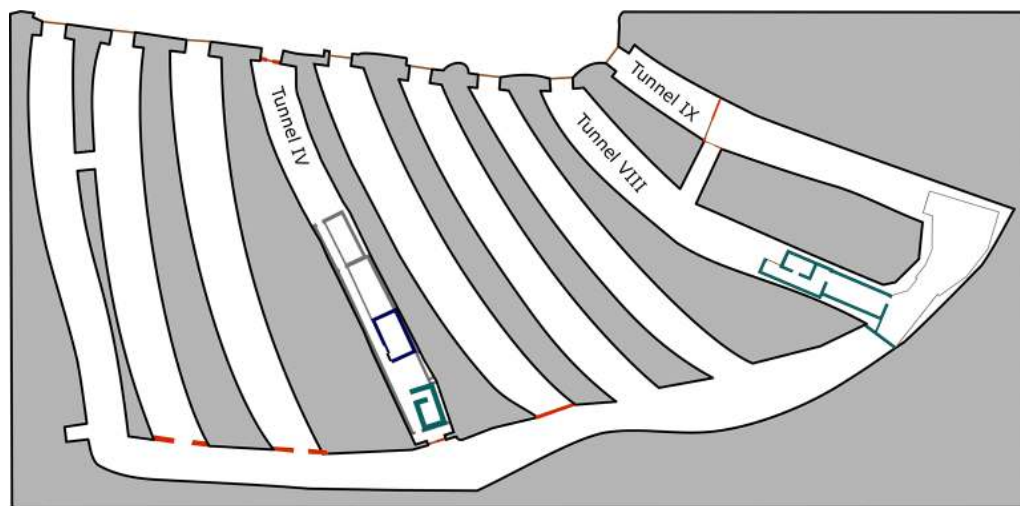
Figure 3.1: Map of the "Felsenkeller" tunnel system. The tunnels containing the particle accelerator and the detectors are VIII and IX.[14]

tunnels consists mainly of hornblende monozyte, which contains ^{138}U and ^{232}Th as sources of radioactivity. The laboratory is mainly known for its tandem pelletron accelerator, but it also contains several other detectors, including the investigated X-ray detector. All detectors are located in so-called "bunkers" with 40cm thick concrete wall floor and ceiling to reduce background radiation from the tunnel walls. The specific activity of ^{238}U and ^{232}Th is in the ranges 14.9-17.8 and 15.6-17.4 Bq/kg, respectively. As shown in figure 3.2he setup used for the experiments in this thesis is build up next to the accelerator behind bunker 111. The setup consists of an X-ray detector with a power supply and a digitizer, which is connected to a laptop to record the data. The detector investigated during the experiments was "SiriusSD®️ Silicon Drift Detector", with a silicon drift sensor that has a detection area 170 mm² area and
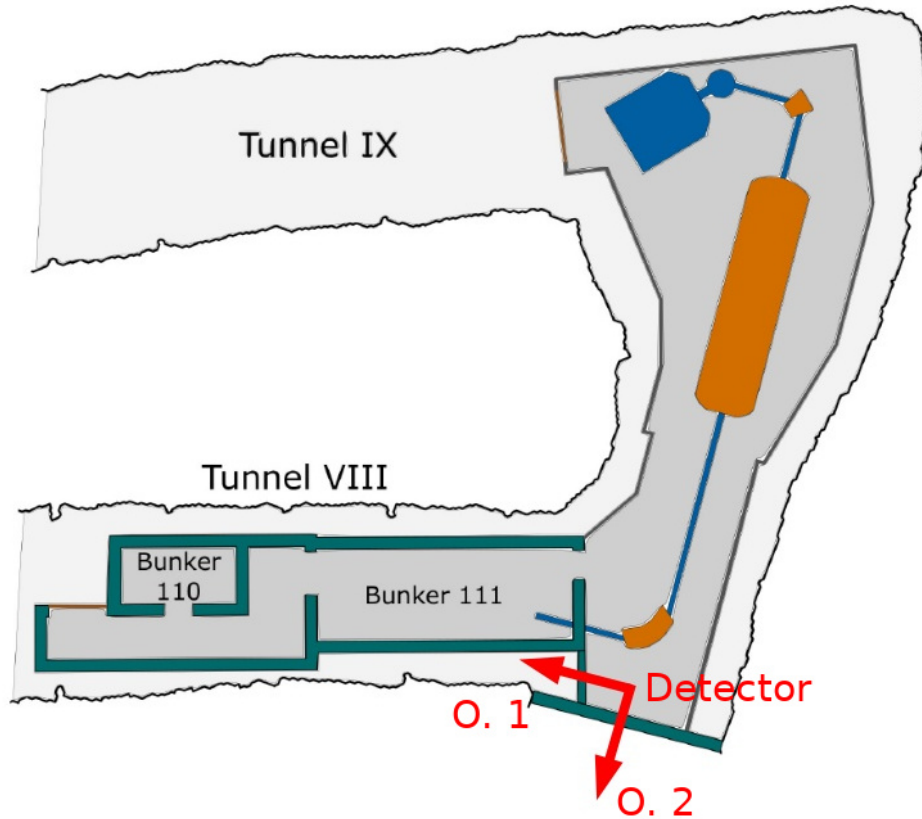
Figure 3.2: Map of Tunnel VIII and IX including the particle accelerator, the bunkers 110 and 111 and the position of the used setup (Detector). The two arrows indicate the window orientation of the detector, with orientation 1 pointing towards the entrance (arrow to left) and orientation 2 pointing perpendicular to the entrance direction (arrow down). [14]

an active thickness of $450\,\mu$m thick. The sensor is covered with a $25\,\mu$m thick Beryllium window. The detector can detect photons with an energy of up to $100\,$keV, but experiments will show that the detector efficiency above $80\,$keV is already too low for sufficient measurements. The resolution given by the manufacturer is $139\,$eV FWHM at $5.9\,$keV.

The head of the detector, which contains the active detector material, as well a collimator and an entrance window, was placed on top of a styrofoam block, which had several cuts to place radiation sources onto it. Two large scintillator panels were also connected to the digitizer to investigate possible muon coincidence between the X-ray detector and the large panels.

The muon panels are the solid scintillation detectors "EJ-200" from "Scionix", each panel has a build-in pmt as well as a build in high-voltage. The size of each panel is 1m×1m×5cm.

The digitizer used for the experiments is a "CAEN DT5725SB" digitizer with 8 possible input nodes. Each node has up to 16384 channels in which the detector entries can be listed. The digitizer runs with the "CoMPASS" software, which can be used for multiple purposes, e.g. for pules height analysis (PHA) and pulse shape discrimination (PSD). In the following, the PHA firmware will be used with its trapezoidal reconstruction algorithm throughout this thesis. The parameters important for the evaluation of the detector signals are the "Input",
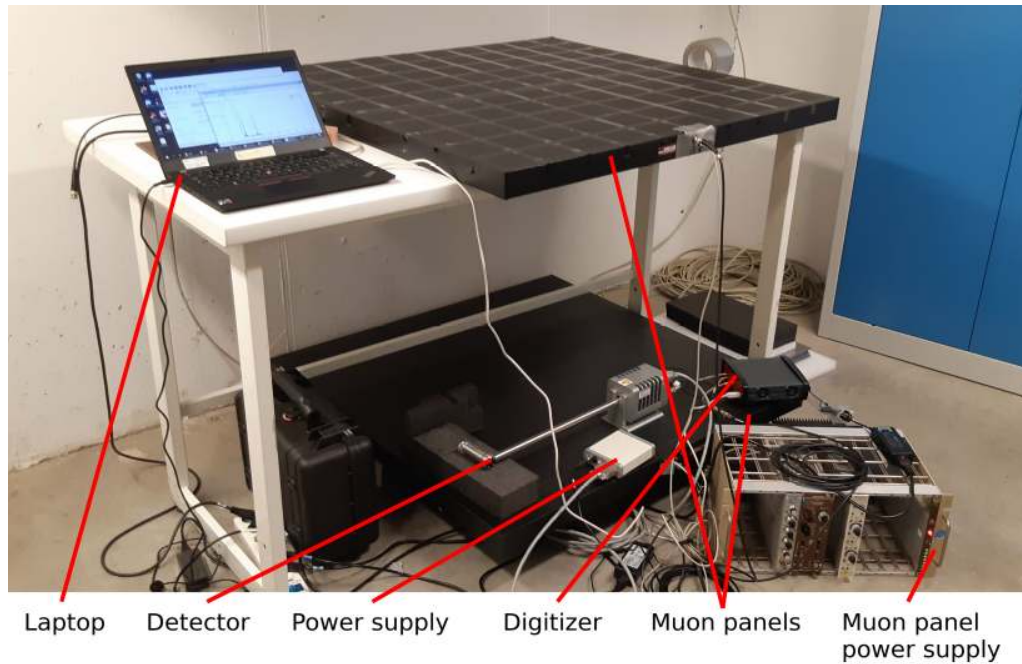
Figure 3.3: Experimental setup consisting of the X-ray detector and the muon panels as well as their power supply and the digitizer. The entrance of the "Felsenkeller" tunnel is to the right on this picture.

the "Discriminator" and the "Trapezoid" settings. The Figures A.2, A.3 and A.4 show the important parameters within the "CoMPASS"-software.

3.2 Radioactive sources and samples

For all the experiments five samples were used, the calibration sources ^{57}Co and ^{133}Ba and three recently activated samples, ^{151}Sm, ^{158}Tb and ^{193}Pt. The three new samples ^{151}Sm, ^{158}Tb and ^{193}Pt are activated with stable samples of the respective elements, which were placed into a neutron field. The neutron field was produced by a DT-generator from the chair of nuclear physics at the TU Dresden and is located at the "Helmholtz Zentrum Dresden Rossendorf" [5]. The flux of the neutron field integrated over the run duration of 4 h is $5.7 \cdot 10^{11} \frac{1}{\mathrm{cm}^2}$, measured at a distance of 10 cm away from the neutron source. The distance between neutron source and target was 20 cm for terbium and platinum and 25 cm for samarium.

- ^{57}Co is a nuclide which decays to the stable nuclide ^{57}Fe via electron capture. This leads to the emission of γ and X-ray lines. Table 3.1 shows the lines relevant for the experiments, as well as the emission probabilities[1]. It is important to mention that these lines are emitted during the excitation of the daughter nucleus. Therefore, an X-ray

---

[1]According to https://www-nds.iaea.org/relnsd/vcharthtml/VChartHTML.html([4]), the probabilities of some X-ray lines are not included there.

source is always accompanied by the X-rays of the daughter nucleus, not the parent nucleus. The half-life of the ^{57}Co nuclide is $T_{1/2} = (271.74 \pm 0.06)\,$d. The source used for the experiments is a point source covered by two layers of polyethylene. Its activity was measured at 1st june 2019 at 00:00 CET, the activity was $A = (28.96 \pm 0.15)\,$kBq.

line type	E/keV^2	emission probability/%
Kα_2	6.3908 ± 0.0016	16.8 ± 0.3
Kα_1	6.4038 ± 0.0016	32.9 ± 0.6
Kβ_1	7.058 ± 0.0016	6.80 ± 0.14
γ	14.4129 ± 0.0006	9.16 ± 0.15

Table 3.1: γ and X-ray lines of interest of ^{57}Co-decay.[1][4][7]

- ^{133}Ba also decays through electron capture to ^{133}Cs (stable), the γ- and X-ray lines of this decay process are shown in table 3.2. The half-life of ^{133}Ba is $T_{1/2} = (10.551 \pm 0.011)\,$y. The source used during the experiments, which is also a point source, had an activity of $A = (13.96) \pm 0.07\,$kBq on the 1st june 2019 00:00 CET.

line type	E/keV^2	probability/%
Lα_2	4.2722 ± 0.0033	
Lα_1	4.2865 ± 0.0033	
Lβ_1	4.6198 ± 0.0033	
Lβ_2	4.936 ± 0.006	
Lγ_1	5.280 ± 0.006	
Kα_2	30.625 ± 0.017	32.6 ± 0.8
Kα_1	30.973 ± 0.017	60.2 ± 1.5
Kβ_1	34.9869 ± 0.017	
γ	53.1622 ± 0.0006	2.14 ± 0.03
γ	80.9979 ± 0.0011	32.9 ± 0.3

**Table 3.2:** γ and X-ray lines of interest of ^{133}Ba-decay.[1][4][7][13][3]

- ^{151}Sm decays via β^--decay to ^{151}Eu. The half-life of ^{151}Sm is (90 ± 8) years. It is an especially interesting nuclide for X-ray analysis because in 99 % of the decays the parent nucleus transfers directly to the ground state without γ-ray emission.

- ^{158}Tb has three district possibilities to decay it can undergo an electron capture, β^+-decay or β^--decay. The daughter nuclei are ^{158}Gd (EC, β^+) and ^{158}Dy (β^-). The probability for EC/β^+-decay is 83.4 ± 0.7 % and the probability for β^--decay is 16.6 ± 0.7 %. The half-life for all decay types is (180 ± 11) years.

---

[2]The uncertainty of energy for an X-ray line is assumed to be equal to its width. [7][13]

[3]The widths of L-X-ray lines of Cs are approximated as the mean value of the widths of L-X-ray lines of Xe and Ba according to [13].

- ^{193}Pt also decays via electron capture to ^{193}Ir with a half-life of (50 ± 6) years. Similar to ^{151}Sm, no γ-ray lines are emitted during the decay.

[4]
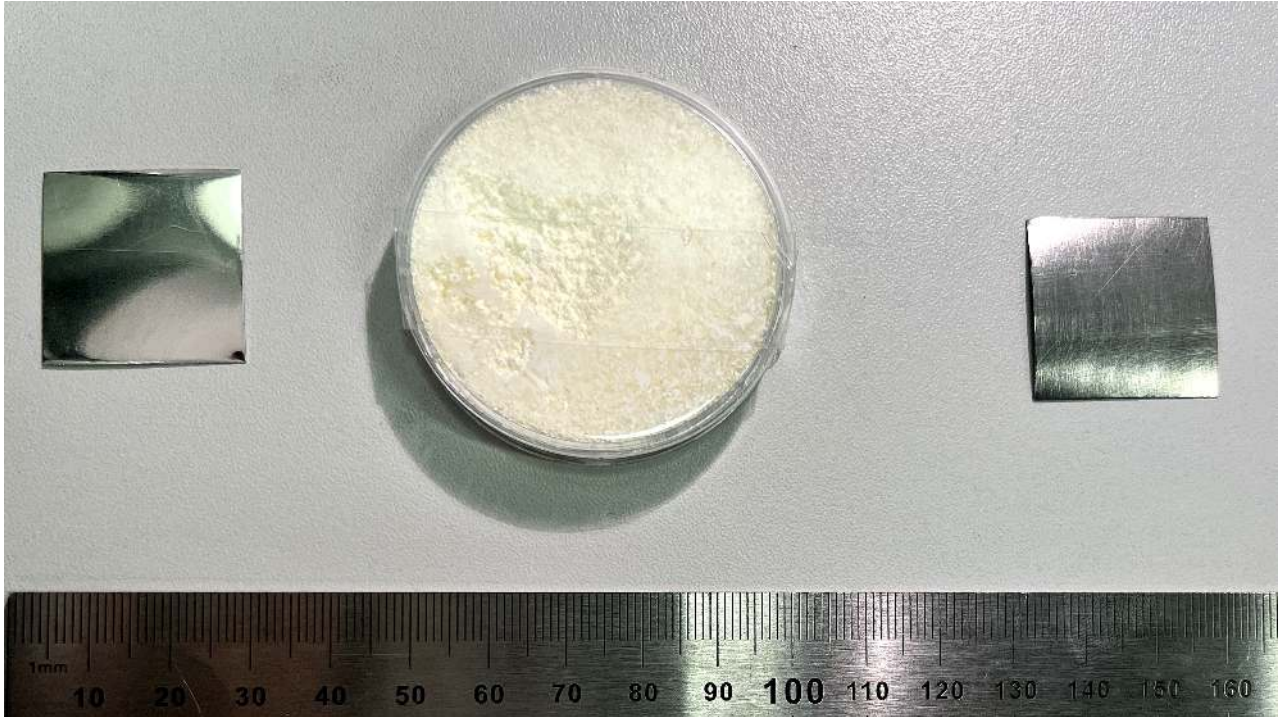
Figure 3.4: The three recently activated samples, from left to right: ^{193}Pt, ^{151}Sm, ^{158}Tb.

4 Results

This chapter is the main part of this thesis, it contains the measurements and data evaluation done with the detector. The first section covers the very first experiments done with the detector, to get a first impression of how measured spectra will look like and whether the detector and digitizer settings are well chosen for any further experiments. After that a section covers the detector orientation, because detector position and orientation may have an influence on the measured background. The third section shows the whether muons have a major influence on the detector. The fourth section covers the detector calibration, which contains the first energy calibration and efficiency calibration for the detector. In the last section the new samples are investigated, which are used in future experiments to determine the half-life of the respective isotopes.

4.1 Test experiments

In order to investigate the detoctor in background conditions and during the measurement of calibration sources, three test runs were performed, which are discussed in the following. The results of these first measurements are shown in the figures 4.1, 4.2 and 4.3.
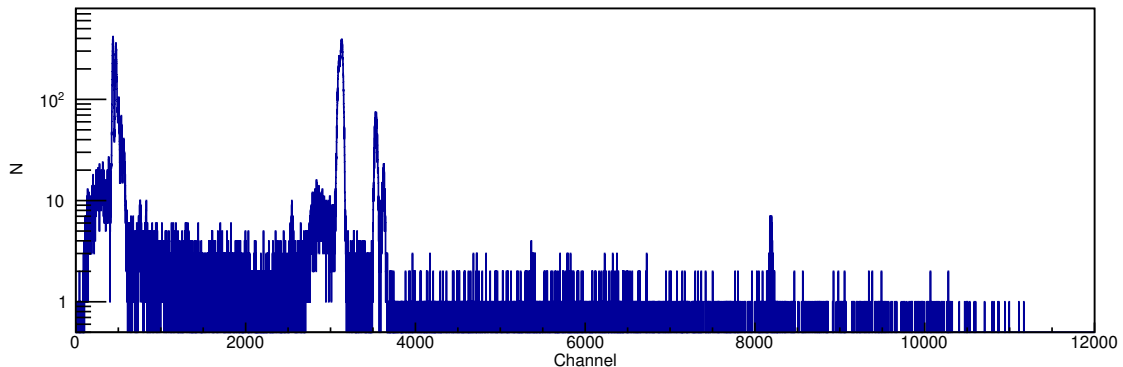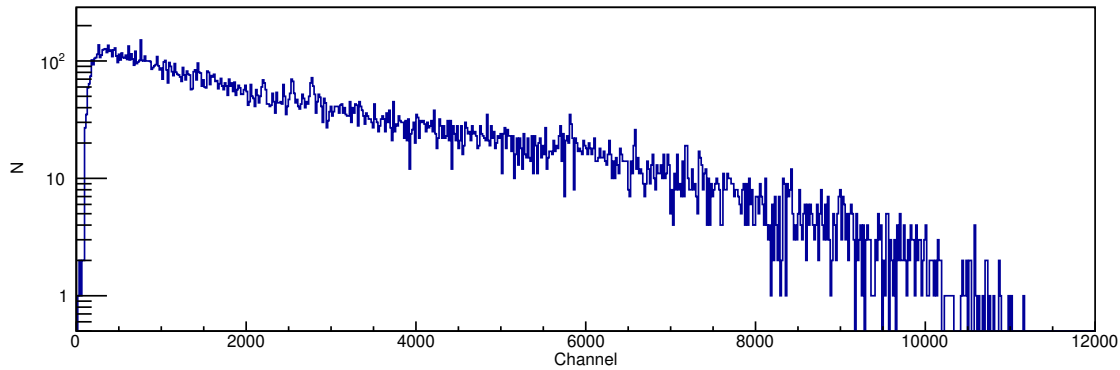

Figure 4.1: Spectrum of ^{133}Ba, detector orientation towards entrance, 05.11.21, 11:20, measuring time [mm:ss]: 32:59.

The first two spectra already show the important γ- and X-ray lines of ^{133}Ba and ^{57}Co decays, which are listed in table 3.1 and 3.2 respectively. The only lines which are almost not visible
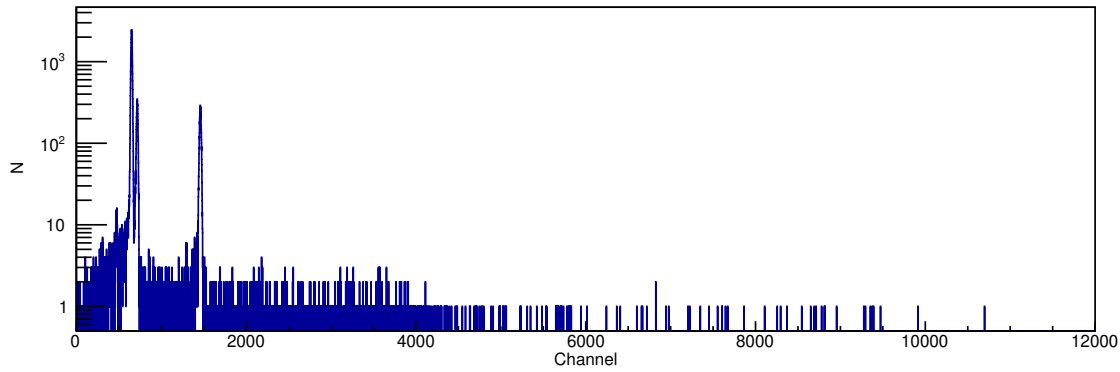
Figure 4.2: Spectrum of ^{57}Co, detector orientation towards entrance, 05.11.21, 11:53, measuring time [mm:ss]: 54:46.

Figure 4.3: Spectrum of background, detector orientation towards entrance, 05.11.21, 12:53, measuring time [hh:mm:ss]: 92:31:42. The spectrum is re-binned by the factor 16 in order to visualize background X-ray lines.

are the γ-ray lines of ^{133}Ba (53 keV & 81 keV). The 53 keV γ-ray line has a comparatively low emission probability, which leads to a small peak slightly above the background (approximately at channel 5300). The 81 keV γ-ray line (approximately at channel 8100) however has a height similar to the 53 keV line, the reason for that is the low efficiency of the detector for energies above 80 keV.

The background spectrum shown in figure 4.3 follows an exponentially decreasing function, which seems typical for low energy background radiation due to the lower detector efficiency at higher energies. When the binning of the background spectrum is changed to a smaller number of bins, several emission lines become visible (three above channel 2000, one below channel 6000). Comparing the γ- and X-ray lines visible in figure 4.1 and 4.2 with the tables 3.1 and 3.2, it can be assumed that 1000 channels are equal to 10 keV. This would lead to the result that the lines in figure 4.3 may be the Kα_1-lines from Sn, Sb and Te and one of the Kα-lines from Ta. These are the materials the collimator consists of, which surrounds the detector sensor to reduce background radiation that is not coming from the window side of the detector.

The test experiments show that the detector measures entries between 0 and 12000 channels, and works sufficient up to channel 8000, excluding the first 100 channels due to the low sensitivity for photons with $\leq 1\,\text{keV}$ energy. This means in conclusion that the detector and digitizer are well set up for any further experiments. The detector records a high amount of signals within a range of 8000 channels, which is sufficient for most experiments, and has a wide channel range to cover eventual high energy signals. The background measurement has measured a total 20060 signals, which results in a counting rate of $60.2 \cdot 10^{-3}\,\text{1/s}$. To investigate how much this rate depends on the detector orientation and on events induced by muons, a second background measurement with a different detector orientation was recorded, which is evaluated in the second experiment. During the measurements of this chapter the detector was oriented towards the entrance of the Felsenkeller, while in the second background experiment as well as in the following experiments the detector was oriented perpendicular to the entrance direction, as shown in the setup picture (figure 3.3).

4.2 Detector orientation

The first main part in the analysis of this thesis is the investigation of the impact of the detector orientation on the background spectrum and its subsequent rate. The "Felsenkeller" laboratory is in a tunnel system with a massive rock overburden. The remaining background radiation consists of photons emitted by materials within the "Felsenkeller" laboratory and cosmic muons, which are the dominant part of remaining cosmic radiation within the tunnels. Their angular distribution has two maxima, namely one pointing to the zenith and one pointing towards the tunnel entrance of the "Felsenkeller" laboratory [9]. To investigate the influence of this effect, the background was measured first with the detector oriented towards the entrance and second with the detector oriented perpendicular to the entrance (figure 4.4a). The expected result should be that the first detector orientation results in a slightly higher background count rate due to the higher muon flux from the entrance, but the counting rate directly induced by photons should not depend on the orientation. The spectra of both experiments are shown in figure 4.5.

The comparison of both spectra already shows that orientation 1 has more entries due to background radiation than orientation 2, especially when the longer measuring time for orientation 2 is considered. To determine how big the difference between both orientations is, the counting rates for each spectrum are determined. The integral of all counts for orientation 1 is 20060 ± 140, which leads to a counting rate of $(60.2 \pm 0.4) \cdot 10^{-3}\,\text{1/s}$. The integral of orientation 2 is much lower with 4730 ± 70 counts, which leads to a counting rate of $(8.84 \pm 0.13) \cdot 10^{-3}\,\text{1/s}$. This means the environmental background rate is decreased by the factor 8 with just changing the orientation of the detector. The reason for the change of counting rate is probably due to the reduce signals induced by cosmic muons. But a reduce of counting rate by the factor 8

(a) Detector oriented towards the entrance of the tunnels, which is located to the right of this picture.

(b) Detector oriented towards the wall of the laboratory, which means particles coming from the entrance side can only interact with a very small detector area.
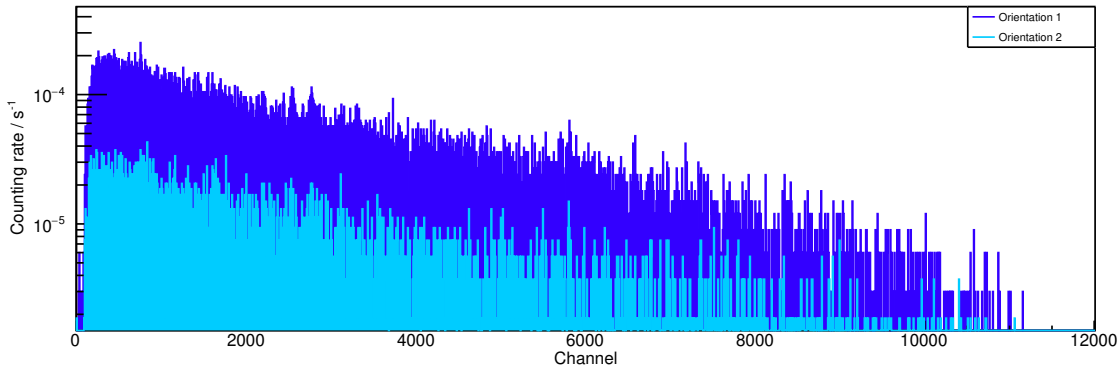
Figure 4.5: Comparison of the background spectra of both orientation: Orientation 1: 05.11.21, 12:53, measuring time [hh:mm:ss]: 92:31:42. Orientation 2: 12.11.21, 11:02, measuring time [hh:mm:ss]: 148:37:33. Both spectra are re-binned by the factor 8.

is far higher than expected, which means there could be other reasons despite the reduce of muon induced signals.

In order to determine whether there was no error during these measurements which lead to the discrepancy, two additional measurements were investigating the stability of the counting rate for orientation 2. The first stability experiment was started on 02.12.2021, with a measuring time of 118:02:41 [hh:mm:ss] and a total number of counts of 28400, which leads to a counting rate of $(66.83 \pm 0.35) \cdot 10^{-3} \, 1/s$. The second experiment started on 21.01.2022 with a total measuring time of 163:00:05 [hh:mm:ss] and a number of counts of 41340, which leads to a counting rate of $(70.45 \pm 0.35) \cdot 10^{-3} \, 1/s$. These experiments with orientation 2 are way more in agreement to the experiment with orientation 1, than the probably faulty first measurement with orientation 2. This leads to the conclusion that the first experiment in orientation 2 most likely suffered from an error during the data acquisition or the analysis. The stability experiments lead to two major conclusions. The first one is that the environmental background is mostly independent of the orientation, with a minor increase in rate for an orientation perpendicular to the tunnel entry. This is an indication that muons may have

less influence on the background rate than expected. Furthermore, the wall of the bunker was closer to the detector within orientation 2, and due to radioactive isotopes within the concrete wall photon background might be created. It can also be noticed that the counting rates of environmental background of the "Felsenkeller" laboratory differs between the last two measurements. A possible reason for the change of counting rate may be a change of concentration of radioactive radon gas in the bunker. But also other reasons like other radioactive materials in the environment of the detector can lead to the instability of the environmental background counting rate.

Despite the results of the stability experiments, which indicate an insignificant influence of muon induced background, it is still important to determine the influence of muons on the environmental background measured by the detector. The next experiment investigates possible coincidences between signals recorded by two large scintillation detectors and signals recorded by the silicon detector. If muons are a dominant source of background in the silicon detector, there should be a clear signal of coincident events between these panels and the SDD.[14]

4.3 Muon coincidence

The previous experiments had the result that the muon induced events within the detector are most likely a minor part of the environmental background, as the detector orientation with a potentially lower muon flux shows the higher counting rate. To verify this theory and investigate how much of an impact muons have on the environmental background, the possible coincidence between entries in the X-ray detector and two muon panels is measured, which are located above and below the SSD (cf. figure 3.3). To do this, both the pulse height of each signal and its time stamp were recorded for the X-ray detector and both panels. After that, for every signal in the X-ray detector the time difference towards the previous and following event in each of the three detectors (the X-ray detector itself and the two muon panels) was calculated. This leads to the timing histogram shown in figure 4.6.

 The upper histogram in figure 4.6 shows the time differences between two subsequent entries in the X-ray detector itself. The space in the middle is created due to the dead time induced by each event. The high number of counts with time differences slightly above the dead time are artifacts due to an undershoot or overshoot of the initial signal, which leads to a subsequent "fake"-event. The lower two histograms show the time differences between events in the X-ray detector and events in the muon panels Sz1 and Sz2, respectively. The diagrams show that there is no time difference appearing far more often than other time differences. When muon coincidence would be significant with respect to the other background events in the X-ray detector, there would be a time difference at or slightly above $0\,\mu$s which appears more often than the other time differences. Since there is no such peak in both histograms in figure 4.6, it can be assumed that the muon coincidence rate is small with respect to the number of
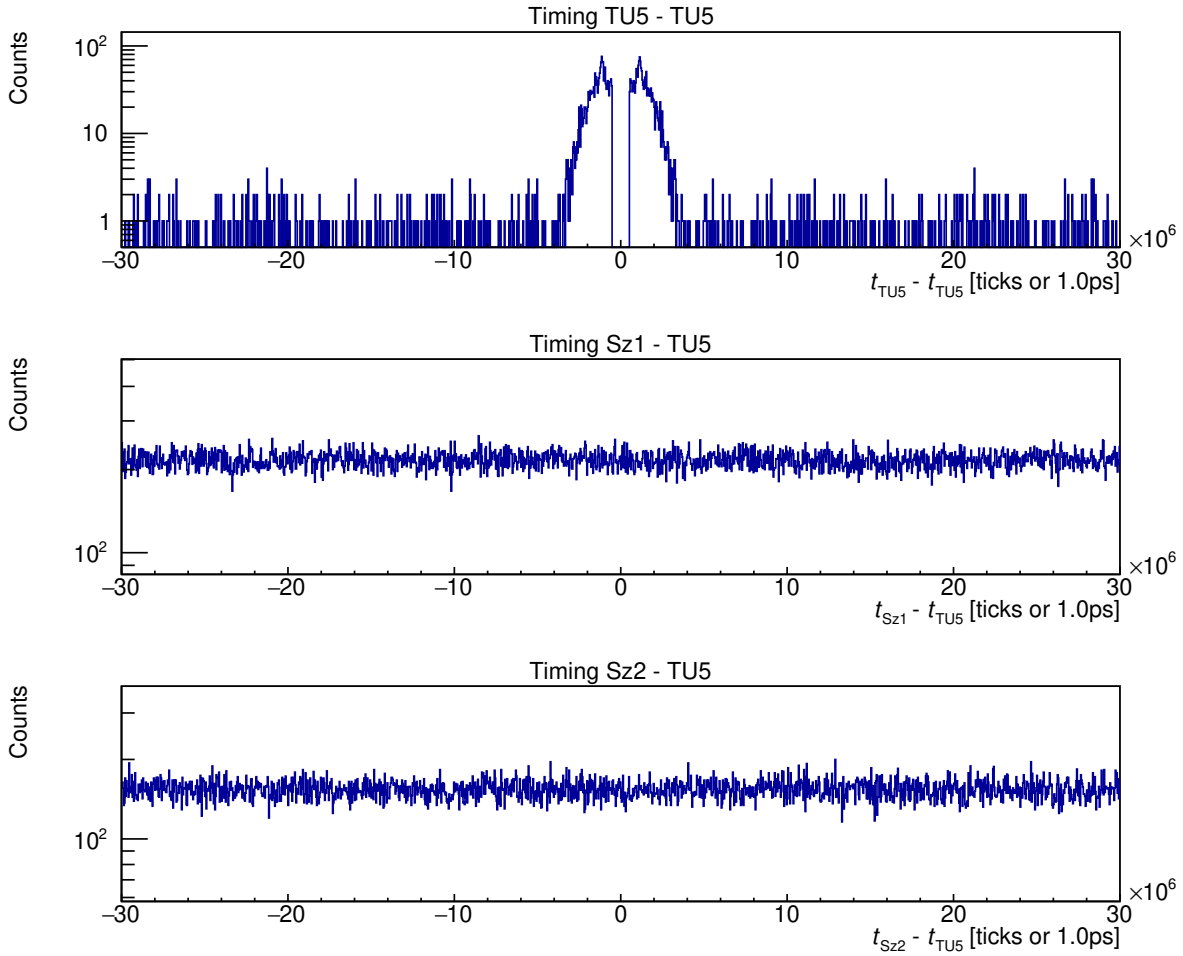
Figure 4.6: Time differences between events in the X-ray detector (TU5) and the respective previous and following event in the X-ray detector and each muon panel (Sz1, top) and (Sz2, bottom).

non-muon induced signals. Therefore it is currently not necessary to write a muon veto script, which would filter entries probably induced by muons, although such a script could become relevent when the background is further reduced with shielding.

Up to this point an energy calibration was not necessary for the experiments, but to investigate γ and X-ray lines emitted by a sample it is now important to make a first detector calibration.

4.4 Detector calibration

An essential part working with detectors is the calibration, which consists of three main parts: the energy calibration the peak width calibration and the efficiency calibration.

Each signal created by a photon is sorted into a specific channel depending on the deposited energy and the signal strength, respectively. The number of channels and the charge range of each channel can vary between different experimental setups and external influences (e.g. temperature). Furthermore, the charge related to a photon energy is also not directly pro-

portional. This means it is almost impossible to determine the energy each channel is related to with just the knowledge about the signal amplifier and digitizer settings. Therefore, the motivation of an energy calibration is to derive the relationship between the channels and their corresponding photon energies.

In order to measure the energy calibration of the detector, the peak positions of several well-known γ- or X-ray lines are determined. Thereby, the chosen full energy peaks should cover the energy range of interest and should be in the first or last $10\,\%$ of the channel range of the detector. With the determined channel C of the peak centroid and the known energy E of the corresponding line, a calibration function can be fitted.

The most common fit function is a linear function of the form

$$E(C)/\,\mathrm{keV} = a + b \cdot C \tag{4.1}$$

with the parameters a and b. This calibration function is on the one hand easy to handle in regard to any data evaluation, on the other hand is a linear function the expected relation between channel number and energy for modern X-ray detectors. Only in a few cases deviations between the data points and a linear calibration occur, which can be compensated by an additional quadratic term:

$$E(C)/\,\mathrm{keV} = a + b \cdot C + c \cdot C^2. \tag{4.2}$$

To determine how well a fitted calibration function matches up with the data points, the reduced χ^2 (χ^2_{red}) is calculated. The χ^2-value of a fitting function is a measure of the quadratic deviations between the data points and the respective function values. The deviations are always determined in units of uncertainty. Thereby, χ^2_{red} compiles to χ^2 divided by the number of degrees of freedom, which is the number of data points minus the number of free parameters. A good value for χ^2_{red} is around 1, whereas a χ^2_{red} above 1 indicates too small uncertainties or not enough parameters, a value below 1 can reveal the opposite.

For the energy calibration the spectra of the ^{133}Ba source and the ^{57}Co source were analyzed. The recorded spectra are shown in figure 4.7 and 4.8.

With some exceptions, the γ- and X-ray lines shown in table 3.1 and 3.2 are used for the energy calibration. The first exceptions are the γ-ray lines of ^{133}Ba, which contain not enough counts for a precise peak approximation. Furthermore, the Kα_1 and Kα_2 X-ray lines of iron which are emitted during the ^{57}Co decay cannot be utilized for the energy calibration since their full energy peaks strongly overlap in the spectrum. To determine the peak positions, normalized Gaussian functions (2.13) were fitted for every peak. In case of an overlap of multiple peaks, the fit function is modified to determine each respective peak position. For the approximation of the background a constant function is used.

The centroids of the used peaks and their respective energies are shown in figure 4.9. The first
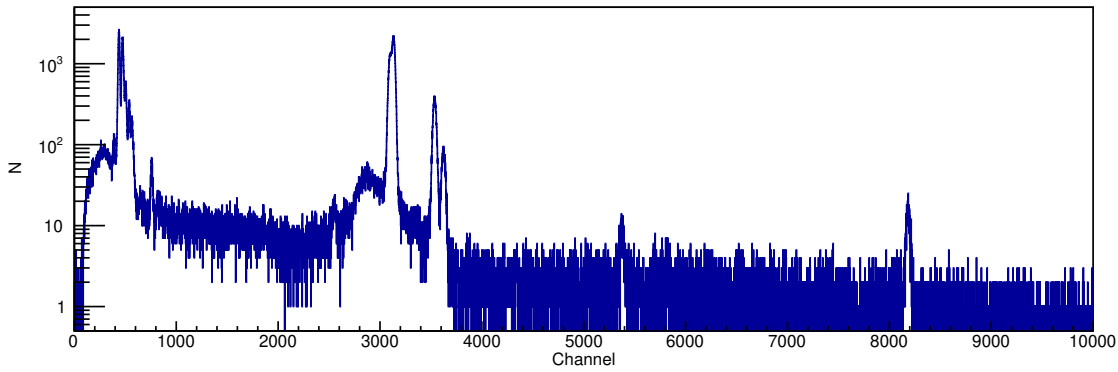
Figure 4.7: Uncalibrated spectrum of the ^{133}Ba source; start: 02.12.21, 14:45; measuring time [mm:ss]: 59:45.
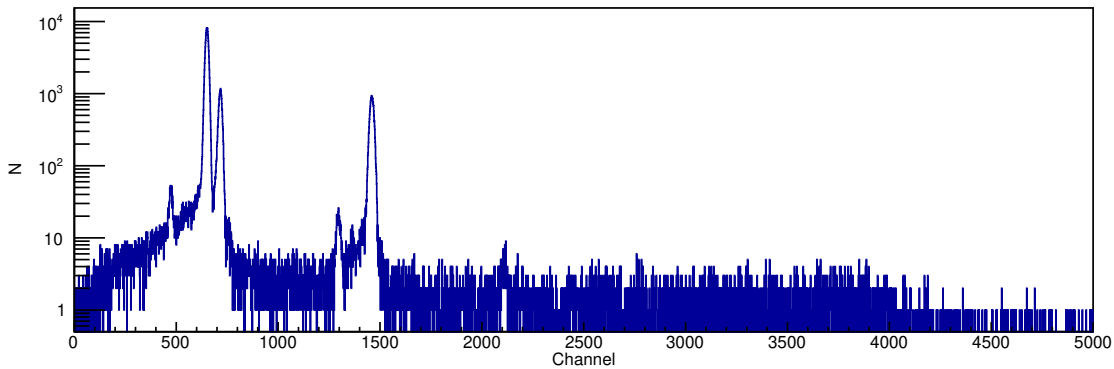
Figure 4.8: Uncalibrated spectrum of the ^{57}Co source; start: 02.12.21, 16:56; measuring time [mm:ss]: 56:41.

calibration function of interest was the linear function (4.1) with the parameters

$$
\begin{aligned}
a &= -0.0423 \pm 0.0022, \\
b &= (9.9024 \pm 0.0017) \cdot 10^{-3}.
\end{aligned}
\tag{4.3}
$$

In order to determine the quality of the fitted function according to the data points, the χ^2_{red}-value of the respective function is determined. The χ^2_{red} value for a linear fit function is:

$$
\chi^2_{red} = 14.10.
\tag{4.4}
$$

This value clearly exceeds the value of 1 which could indicate a wrong function. In order to prove this, function (4.2) is tested as fit function function. The respective parameters for (4.2)

are determined:

$$a = -0.0465 \pm 0.0034$$
$$b = (9.911 \pm 0.005) \cdot 10^{-3} \qquad (4.5)$$
$$c = (-3.5 \pm 2.1) \cdot 10^{-9}$$

To determine the degree of deviation between this function and the data points, the respective χ^2_{red}-value was calculated:

$$\chi^2_{red} = 15.99 \qquad (4.6)$$

This χ^2_{red}-value is just slightly higher than the χ^2_{red}-value of (4.1), which indicates that a quadratic fit function has deviations from the data points similar to a linear fit function. Reason for that is that the parameter c, which accords to the quadratic term in (4.2), is very small. At channel 1000, which is around $10\,\text{keV}$, is the quadratic term around $4\,\text{eV}$ high. In comparison to that is the uncertainty of c, which is $50\,\%$ of c itself. Thus it can be assumed that the parameter c is negligible. The calibration function chosen for further experiments is therefore the linear fit function (4.2) shown in figure 4.9, even so the χ^2_{red}-value is clearly above 1. The reason for such a high χ^2_{red}-value is probably that the data points from the X-ray
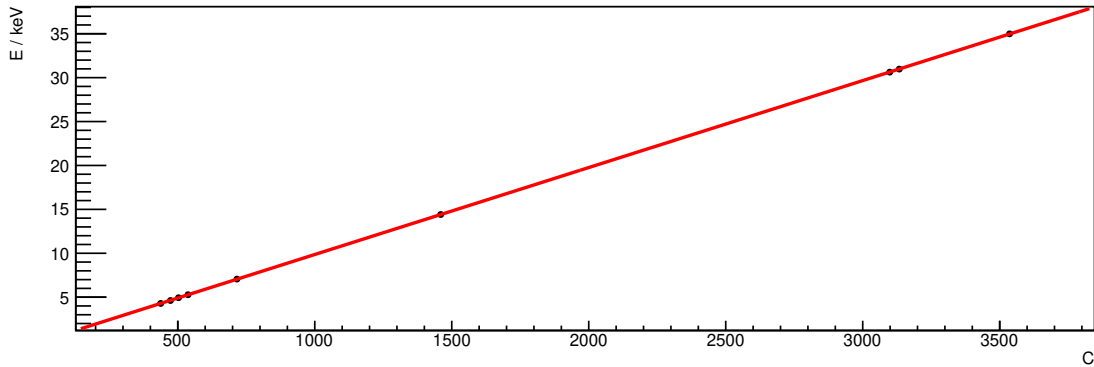
Figure 4.9: Calibration points in an $E(C)$ diagram, with the linear fit function as respective calibration function. The deviations between the function and the data points as well as the respective uncertainties are comparatively small and therefore not visible in this diagram.

lines had to be evaluated as bunches of multiple Gaussian functions. This may lead to higher uncertainty for the peak centroids produced by the tailing of secondary X-ray lines. That indicates that more single lines have to be measured and evaluated in order to determine the correct calibration function for this detector setup. Especially low energy γ-ray lines could improve the calibration due to their low width. For now, function (4.1) with the respective parameters (4.3) is the best calibration function available so far. It will be used for the investigation of the new samples. Another problem of this calibration function is that only data points with energies below $35\,\text{keV}$ are used, so above 35 keV this function can only be

approximated as a correct calibration function.

A secondary part of the detector calibration is the investigation of the widths of lines compared to their energy. The peak widths (FWHM) are determined for each calibration point, which leads to figure 4.10. This diagram shows the energy resolution depending on the energy of each point. The theoretical function for the width of a recorded line is

$$\text{FWHM}(E)^2 = W_E^2 + W_X^2 + W_D^2, \tag{4.7}$$

with the width created by electronic noise W_E and the width created by leakage current W_X, which is almost zero for small detectors. W_D is the width created by the signal production, since the number of charges created by a measured photon has a statistical error. This width is $W_D^2 = 2.35^2 \cdot \varepsilon \cdot F \cdot E$, with ε being the energy necessary to lift an electron into the conduction band and the Fano-factor F. Since W_E, ε and F are constant, the FWHM can be expressed as

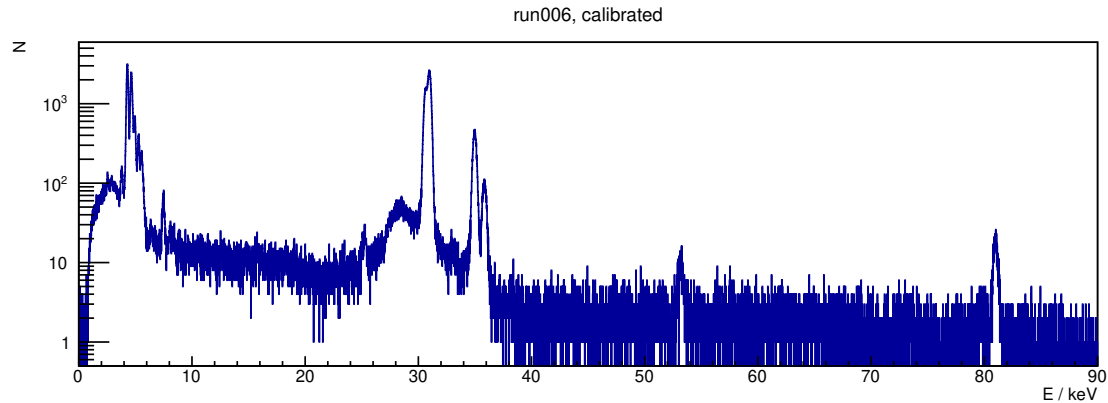$$\text{FWHM}(E)/\text{kev} = a \cdot \sqrt{E + b}. \tag{4.8}$$

With the data points shown in figure 4.10 the parameters a and b can be determined.

$$\begin{aligned} a &= 0.0542 \pm 0.0003 \\ b &= 4.69 \pm 0.14 \end{aligned} \tag{4.9}$$
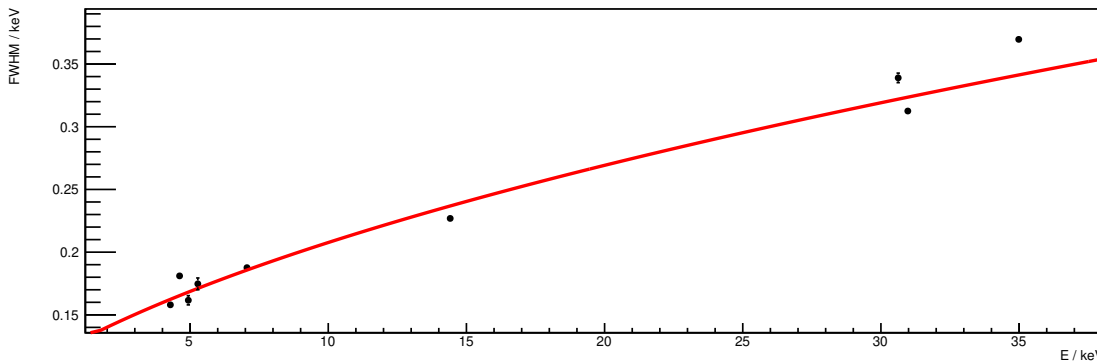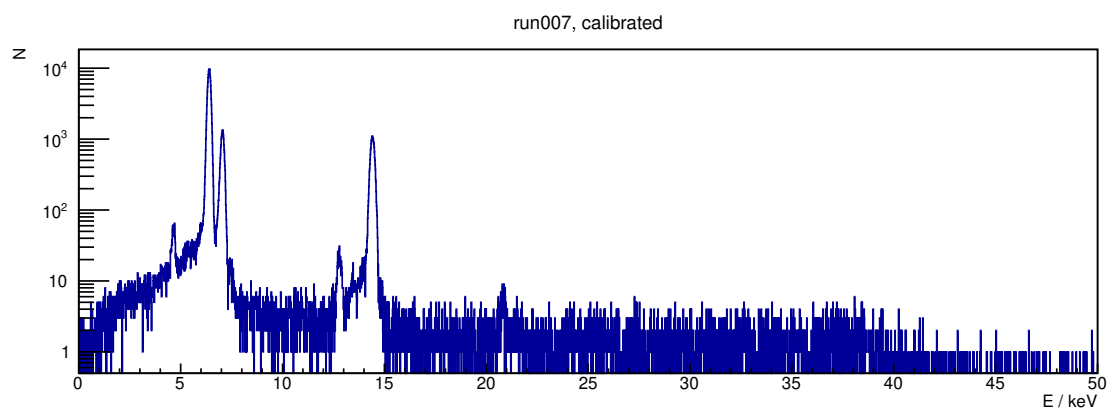

Figure 4.10: FWHM of calibration peaks depending on E with resolution function.

To give an example of what an energy calibrated spectrum looks like, figure 4.11 and 4.12 show the calibrated ^{133}Ba and the ^{57}Co spectrum.

Figure 4.11: Calibrated ^{133}Ba spectrum.

Figure 4.12: Calibrated ^{57}Co spectrum.

The efficiency calibration is necessary for the determination of absolute activities. A detector only measures a small amount of photons of a certain energy emitted by a source. There are three main reasons for this:

- The geometry of detector and source, because only a certain amount of radiation is directed towards the detector.

- Emitted radiation can interact with the matter between detector and radiation source. Due to these interactions a part of the emitted radiation cannot reach the detector or loses energy due to scattering.

- When radiation interacts with the detector material, there is a chance that the recorded energy does not correspond to the energy of the radiation due to various escape effects (cf. section 2.5.1).

Since the last two parts depend heavily on the photon energy, the efficiency of the detector must be measured over its energy range.

The determined efficiency is the absolute full energy peak efficiency $\epsilon(E)$, which is the probability that a photon emitted by a fixed sample deposits its full energy in the detector. The

absolute full energy peak efficiency relates the number of counts in a full energy peak N to the number of photons of the respective line emitted by the sample. The absolute full energy peak efficiency is

$$\epsilon(E) = \frac{N_d}{\nu \cdot A \cdot t_{\mathrm{L}}} \tag{4.10}$$

with the activity of the sample A, the emission probability ν and the dead time corrected measuring time, called life time t_{L}. It must be noted that this function only applies when $t_{\mathrm{L}} \ll T_{1/2}$, or else A must be integrated over t_{L} do determine the number of decays during the experiment. The full energy peak efficiency consists of three factors, the detector efficiency ϵ_d, the geometric efficiency of the setup ϵ_g and the efficiency of the source ϵ_s:

$$\epsilon = \epsilon_d \cdot \epsilon_g \cdot \epsilon_s. \tag{4.11}$$

especially the last two are hard to calculate and may carry high uncertainties, so it is more useful to just measure the full energy peak efficiency instead of determining the different parts of the efficiency by themselves.

For this calibration, only the lines with known probabilities were used. One exception were the $K\alpha$-lines of Fe from the ^{57}Co-decay due to their strong overlap, as mentioned previously. Due to the rarity of low energy γ-ray lines only one γ-ray line of ^{57}Co was included. The area of each peak was determined by fitting a normalized Gaussian function (2.13) for the respective peak, the background was assumed with a constant function and secondary peaks were determined with subsequent Gaussian functions. This leads to the detector efficiency depending on the energy of the line as shown in figure 4.13. This diagram indicates well that the detector efficiency decreases linearly, the reason for that is the decreasing cross-section of photoelectric effect and Compton effect at higher energies.
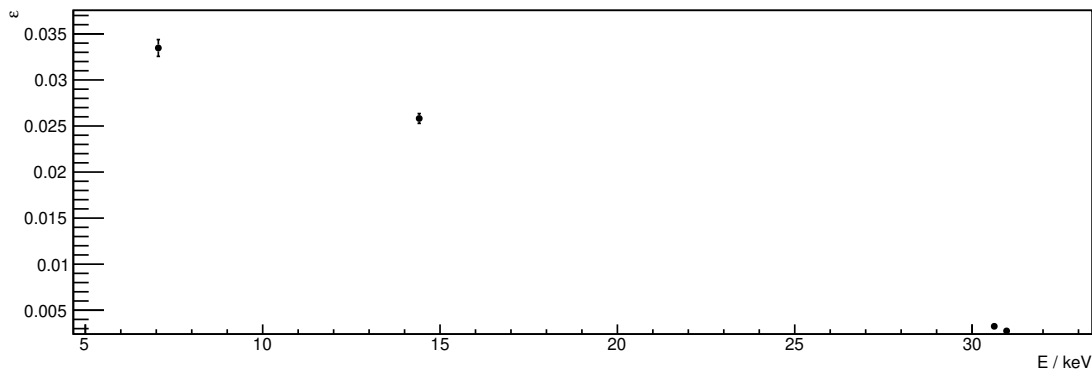
Figure 4.13: Full energy peak efficiency depending on energy.

Stability experiments

In order to determine the stability of the detector regarding to the energy calibration, spectra for the calibration sources ^{133}Ba and ^{57}Co were recorded for a second time after finishing the primary measurements. The peak centroids determined by Gaussian fits are compared between both calibration campaigns (02.12.2021 and 21.01.2022). The peak centroids for their respective lines are listed in table 4.1. The second calibration campaign resulted in lower peak centroid positions compared to the first calibration campaign. Especially for low energy peaks deviations of up to 1 channel occurred. A deviation of 1 channel leads to an energy deviation of 0.01 keV. Peaks at higher energies had smaller deviations comparable to the uncertainty of the peak position.

| nuclide	line type	E/keV	μ(02.12.2021)	μ(21.01.2022)
^{133}Ba	Lα_1	4.287 ± 0.003	437.635 ± 0.040	436.78 ± 0.05
	Lβ_1	4.6198 ± 0.003	473.36 ± 0.06	472.62 ± 0.07
	Lβ_2	4.9359 ± 0.006	502.84 ± 0.14	502.07 ± 0.19
	Lγ_1	5.2804 ± 0.006	537.38 ± 0.20	536.44 ± 0.24
	Kα_2	30.6251 ± 0.017	3098.54 ± 0.29	3098.58 ± 0.38
	Kα_1	30.9728 ± 0.017	3133.50 ± 0.17	3133.42 ± 0.22
	Kβ_1	34.9869 ± 0.017	3536.01 ± 0.14	3536.18 ± 0.17
^{57}Co	Kβ_1	7.058 ± 0.0016	715.97 ± 0.06	715.66 ± 0.09
	γ	14.4129 ± 0.0006	1459.82 ± 0.07	1459.42 ± 0.10

Table 4.1: Comparison of peak centroid positions μ of the calibration peaks between both calibration campaigns.

4.5 Investigation of new samples

Detector setup and characterization shall now be applied in the investigation of three new, recently activated samples. The activation process is briefly described in section 3.2. The half-lives of the new samples are also mentioned in section 3.2, but all three half lives have a high uncertainty between 6 % and 12 %. This leads to the motivation to determine the half-lives of these samples with higher accuracy, but the time necessary to reach this goal goes beyond the time for this thesis. Therefore only first investigation measurements in order to prepare accurate half-life experiments were done in this thesis.

There are two methods to determine the half-life of a radioactive nuclide. For low half-lives the activity of the source is measured several times over a long time, and the half-life can be determined by the activity loss of the source ($A = A_0 \cdot \mathrm{e}^{-\lambda \cdot t}$). In this approach the half-life is extracted from the quotient of activities. The detector efficiency applies linear to the activity, which means the detector efficiency and its systematic uncertainty cancel out in the calculation of the half life (with the assumption that the efficiency is constant over

thee time of the experiment). For high half-lives the activity is measured, and with the full energy peak efficiency and the number of atoms of the investigated isotope the half-life is determined ($A = \lambda \cdot N$). But for half-lives between 20 and 200 years neither one of these methods is sufficient. Therefore the long term goal is to determine these half-lives with higher
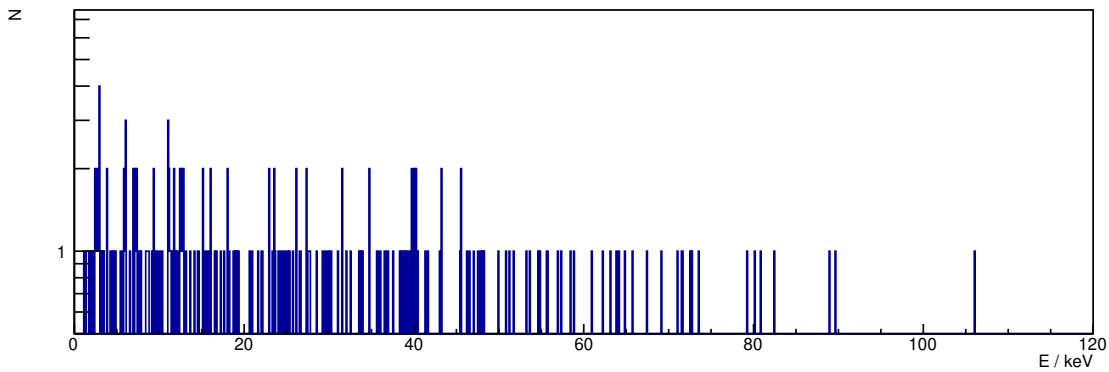
Figure 4.14: Measured spectrum of ^{151}Sm, start: 10.12.21 14:58, measuring time [hh:mm:ss]: 1:00:00. This spectrum is re-binned by the factor 10.

precision, which includes that a suitable method for precise half-life measurements for these isotopes has to be found. The first measurements mentioned in this chapter shall measure the order of magnitude of activity and shall determine problems that may occur during half-life measurements for the respective isotopes.
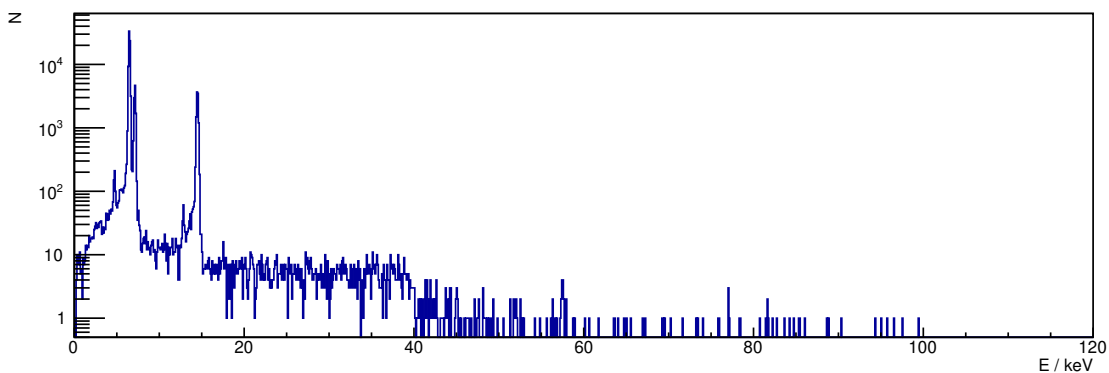
Figure 4.15: Comparable spectrum of ^{57}Co, start: 10.12.21 10:31, measuring time [hh:mm:ss]: 1:00:00. This spectrum is re-binned by the factor 10.

The first spectra recorded were measurements with a real time of one hour. Figure 4.14 shows the spectrum of the ^{151}Sm sample, while figure 4.15 is a comparable spectrum of ^{57}Co. The other two samples, ^{193}Pt and ^{158}Tb, have spectra similar to figure 4.14. The three spectra show a really low rate of entries, almost comparable with the environmental background. This means the activity of the new samples is extremely low, so measurements over several days are necessary to measure lines that may be related to the decay of these samples. Another improvement would be to increase the number of investigated isotopes, which will be discussed later.

In a next step a second measurement was recorded for each sample with measurement times of several days. The recorded spectrum for ^{151}Sm is shown in figure 4.16). Due to the longer
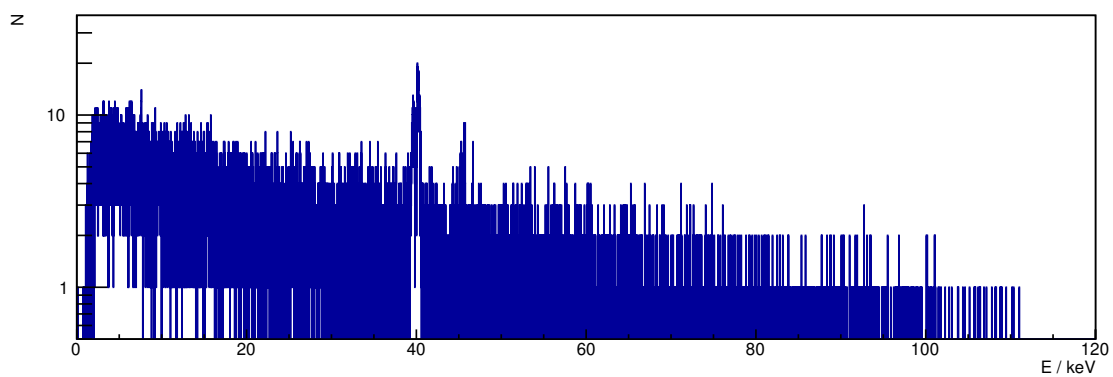
Figure 4.16: Measured spectrum of the ^{151}Sm sample, start: 10.12.21 16:12, measuring time [hh:mm:ss]: 73:13:39.

duration of the measurement X-ray lines were visible, especially two lines around 40 keV, which are shown in detail in diagram 4.17. The energy of the lines are 39.537 ± 0.017 keV
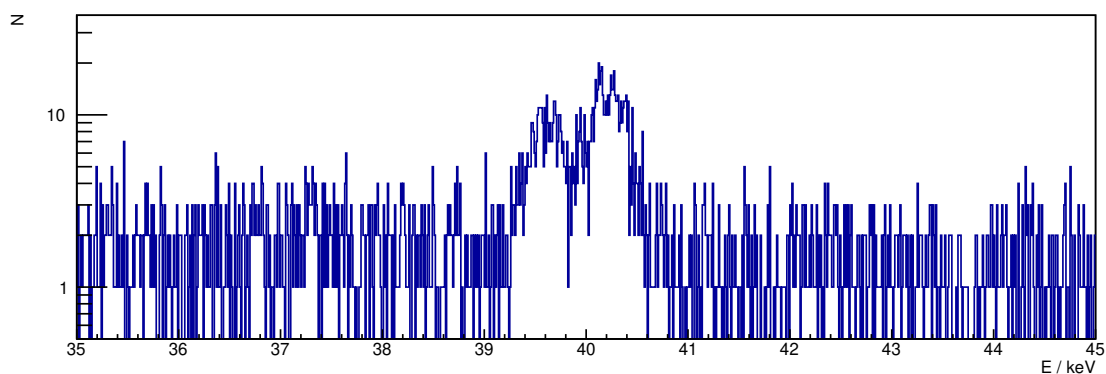
Figure 4.17: ^{151}Sm spectrum as shown in fig. 4.16, close-up on the lines of interest.

and 40.132 ± 0.012 keV. When ^{151}Sm decays, the expected X-ray lines are the X-ray lines from ^{151}Eu, namely Kα_1 with 41.542 keV and Kα_2 with 40.902 keV [1]. The difference in energy between these two lines and the recorded lines is between 90 and 120 times the uncertainty

of the recorded lines. This means the recorded lines are not created by decay of ^{151}Sm nuclei. Since the sample consists mostly of samarium, the measured peaks probably accord to the Kα_1 and Kα_2 lines of ^{151}Sm, which are at 40.118 keV and 39.522 keV and match the measured lines with higher probability because the peak position deviation is in the order of magnitude of uncertainties. ^{151}Sm lines can only have two causes. The first one is that during the activation of the samples with a neutron field, an isotope was created which decays into samarium and therefore leading to those X-rays. The created isotope must have a half-life of multiple weeks at least, since the samples were activated on the 14th of October 2021, eight weeks before the measurement. Possible interactions between a nucleus and a fast neutron are:

$$_Z^A\text{X} + \text{n} \rightarrow _Z^{A+1}\text{X} + \gamma \tag{4.12}$$

$$_Z^A\text{X} + \text{n} \rightarrow _Z^{A-1}\text{X} + 2\text{n} \tag{4.13}$$

$$_Z^A\text{X} + \text{n} \rightarrow _{Z-1}^{A}\text{W} + \text{p} \tag{4.14}$$

$$_Z^A\text{X} + \text{n} \rightarrow _{Z-2}^{A-3}\text{V} + _2^4\alpha \tag{4.15}$$

These reactions are called (n, γ), (n, 2n), (n, p) and (n, α). The only isotope that decays into samarium and has a sufficiently long half-life is ^{147}Pm, which could be created with ^{147}Sm (n, p) ^{147}Pm.

The second possible cause for the X-ray lines of ^{151}Sm is X-ray fluorescence (XRF), which means that the electrons in the atomic shell of samarium are excited via interaction with background radiation. The atoms deexcite, leading to the characteristic X-ray lines of the sample material. Which of these causes for the X-ray lines of the original sample material is the more likely one can be determined by investigating the other samples.

The second investigated sample was ^{193}Pt, its spectrum is shown in figure 4.18, the interesting peaks are shown in figure 4.19. The interesting peaks are at the energies 9.439 ± 0.008 keV
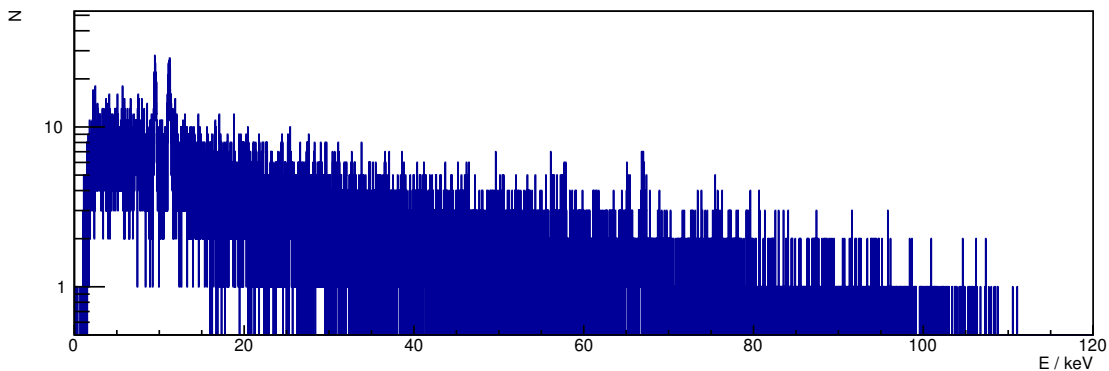
Figure 4.18: Measured spectrum of the ^{193}Pt sample, start 12.01.22 9:26, measuring time [hh:mm:ss]: 125:01:26.

and 11.106 ± 0.010 keV. The closest X-ray lines to these would be the Lα_1, Lα_2 and Lβ_1 lines of platinum, which are 9.442 keV, 9.362 keV and 11.071 keV. These lines are closer to the
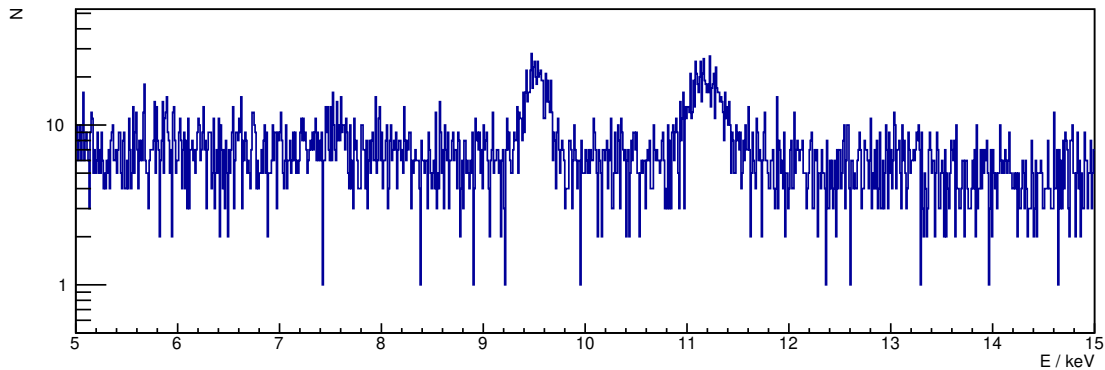
Figure 4.19: ^{193}Pt spectrum as shown in fig. 4.18, close-up on the lines of interest.

experimental results than the $L\alpha_1$, $L\alpha_2$ and $L\beta_1$ lines of iridium, which should be produced during the decay of ^{193}Pt. This means again that either isotopes decaying to platinum are produced or XRF is visible. The first cause is very unlikely, because the only producible isotope with a sufficiently high half-life and a decay into platinum is ^{192}Ir. This isotope could be created via ^{192}Pt (n, p) ^{192}Ir, but since this platinum isotope is not appearing often (0.7% abundance[1]), this is probably not the cause for the platinum X-ray lines in the spectrum. This means XRF is the most probable reason for the X-ray lines, and regarding the investigation of the half-lives of the radionuclides XRF has to be negated. To show if XRF is most likely the reason for the X-ray lines, the last sample ^{158}Tb has to be investigated.

The spectrum of the ^{158}Tb sample is shown in figure 4.20.
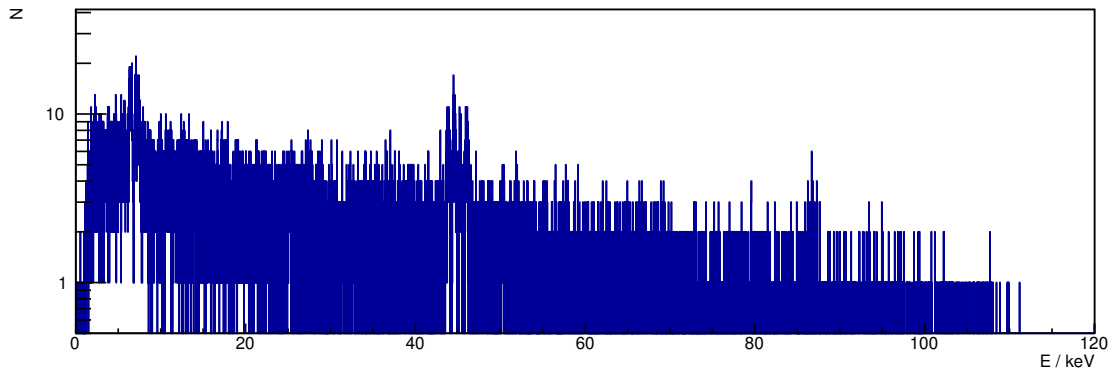
Figure 4.20: Measured spectrum of the ^{158}Tb sample, start: 17.01.22 18:34, measuring time [hh:mm:ss]: 44:50:57.

Two bunches of peaks are visible in this spectrum, they are shown in detail in figure 4.21 and 4.22, respectively. However, the first bunch of peaks around 7 keV consists of several closely spaced X-ray lines with low count rates, which makes a qualitative analysis difficult. The X-ray lines at about 40 keV are more distinguished and can be evaluated with Gaussian fits. The resulting energies are 43.781 ± 0.021 keV, 44.494 ± 0.015 keV, 45.227 ± 0.025 keV and

---

[1] [4]
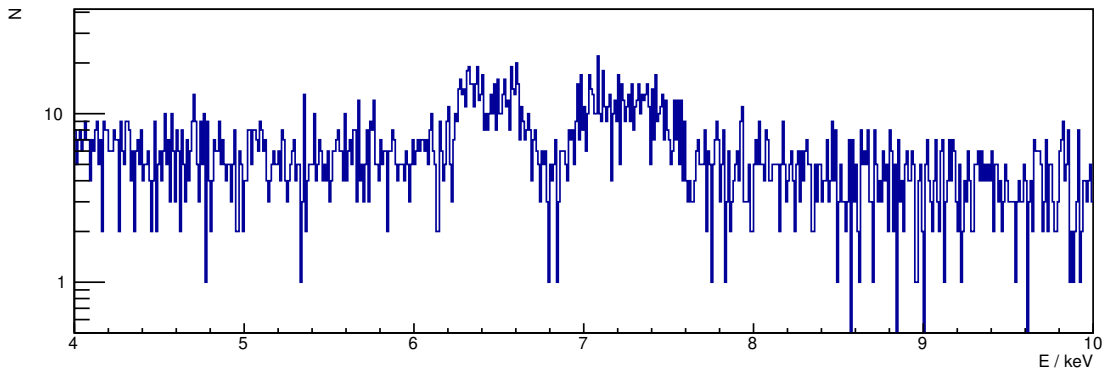
Figure 4.21: ^{158}Tb spectrum as shown in fig. 4.20, close-up on the lines of interest (4-10 keV).
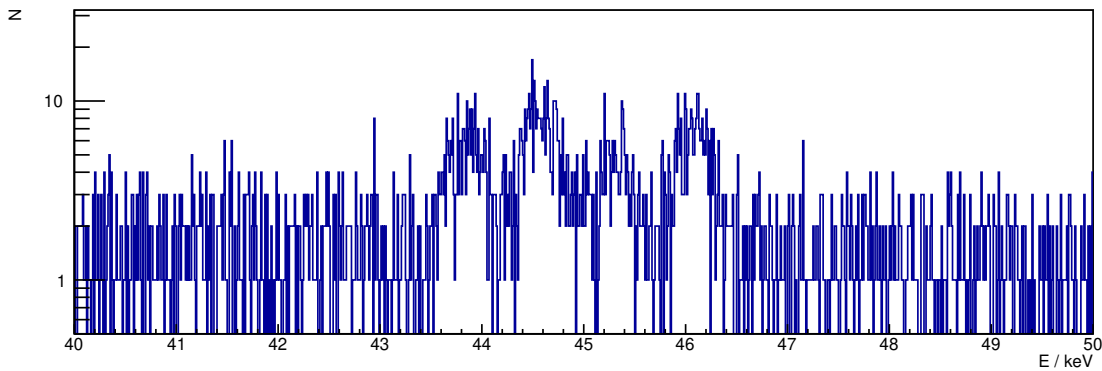
Figure 4.22: ^{158}Tb spectrum as shown in fig. 4.20, close-up on the lines of interest (40-50 keV).

46.022 ± 0.017 keV. Candidates for these X-ray lines are the Kα_1 and Kα_2 lines of gadolinium, terbium and dysprosium shown in table 4.2. That means the X-ray lines correspond to ter-

Element	Line	Energy/keV
Gd	Kα_1	42.996
	Kα_2	42.309
Tb	Kα_1	44.482
	Kα_2	43.744
Dy	Kα_1	45.988
	Kα_2	45.208

Table 4.2: Canidates for the X-ray lines visible in figure 4.22

bium and dysprosium. The reason for the terbium X-ray lines must be XRF, because there are no isotopes creatable with fast neutrons which have a sufficiently long half-life and decay into terbium. It is also very likely that the X-ray lines of samarium and platinum result from XRF, so negating XRF is a major goal before half-lifes can be measured.

^{158}Tb decays to $83.4\,\%$ into ^{158}Gd and to $16.6\,\%$ to ^{158}Dy, and since no X-ray lines of gadolin-

ium are visible, the X-ray lines of dysprosium cannot come from this decay. Looking at the possible interactions between neutrons and nuclei, the possible isotopes that were created by the neutron reactions are ^{158}Tb and ^{160}Tb. The isotope ^{160}Tb decays via β^--decay into ^{160}Dy and ^{160}Tb has a half-life of 72.3 days. That means if both isotopes were produced in equal amounts during the irradiation, ^{160}Tb would have 900 times the activity of ^{158}Tb. The cross section of (n, γ) is by a factor of about 1000 smaller than the cross section of (n, 2n), which means $A(^{160}\text{Tb})/A(^{158}\text{Tb})$ is approx. 0.9. So there must be an additional explanation for the dysprosium X-ray lines. Since it is very unlikely that the terbium foil was not clean before activation, the only explanation that comes in mind is XRF of dysprosium, but this is just speculation. To determine whether this may be the reason for the dysprosium X-ray lines to appear in this magnitude, experiments with or without shielding to reduce XRF have to be compared.[1][4]

5 Summary and Outlook

The aim behind this thesis was in the first place the development of a low background detection setup, which should be sensitive to low energetic gamma-radiation and X-rays. Such a setup would enable precise half-life measurements of samples with low activities, γ-ray lines of low emission probabilities and low energetic γ-rays.

Indeed, the counting rate in the detector varied insignificantly for different detector orientations which indicated that muons do not have any influence to the spectrum. Until now, only two different detector orientations were investigated. In order to determine the detector orientation which causes the smallest amount of background, further measurements with more orientations should be implemented. The influence of the bunker walls should also be investigated in further experiments by varying the distance between X-ray detector and wall or by implementing shielding between wall and detector.

The results of the orientation-dependent background experiments indicated no significant muon-induced background. Nevertheless, it should be excluded if muons have any impact to the measurement. For this reason, a muon coincidence setup was constructed. Again, the experimental results showed no evidence if muons cause any background. One reason for this might be that the detector window is orthogonal to the muon panels, so muons have a low probability of passing the detector window. Furthermore, the large distance between the muon panels and the detector as well as the large difference between the detector sizes further decrease the probability that a muon passes through all three detectors. The distance between the muon panels can not vary in the used setup. To improve this measurement, a muon coincidence setup with smaller, freely positionable muon panels is necessary. Such a setup would maybe lead to muon coincidence, which can be eliminated and thus reduce the background even more. In addition, further muon coincidence measurements with the muon panels placed parallel to the detector window would be useful.

The next part was the calibration of the detector. The energy calibration with a linear function did not match up very well with the data points according to the χ^2-value of the function. The attempt to improve the calibration function by adding a quadratic term did not lead to a significant improvement in regard to the χ^2-value, which lead to the linear function as calibration function of choice. The energies of the full energy peaks of the three recently activated samples ^{151}Sm, ^{193}Pt and ^{158}Tb determined by the Gaussian approximation showed deviations from the literature values [1] of up to three times the uncertainty. To improve the energy

calibration, it is necessary to have more isolated γ- and X-ray lines for low energies, because a major problem for the peak centroid determination was the influence of lines close to the respective analyzed peak. A major improvement of the detector calibration would be given by additional sources with γ-ray lines from about 5 to 80 keV. Unlike X-ray lines, γ-ray lines are usually distinguished from other lines and therefore usually occur as single peaks. Alternatively, the 53 keV and 81 keV γ-ray lines can be added to the detector calibration if the ^{133}Ba sample is measured for a longer period in order to increase the statistic of both peaks. Another improvement that could be possible, but needs further theoretical research, is to express γ- and X-ray lines by more complex functions to have a better consideration of the tailing on both sides of the peak. The last improvement necessary for an optimized energy calibration is to recalibrate the X-ray detector over time due to minor instabilities of the detector.

The last main results were obtained by the first investigations of the pulse height spectra of three samples, which were activated by 14 MeV neutrons generated by a DT generator. The nuclides of interest were ^{151}Sm, ^{193}Pt and ^{158}Tb. In each of the three recorded spectra only the X-ray lines of the respective samples were visible, the reason for these lines to appear was probably X-ray fluorescence. The X-ray lines of the respective daughter nuclides were not present within the spectra. Only the spectrum of the terbium sample showed X-ray lines of dysprosium, but these lines probably also come from XRF. To reduce this effect and the background in general even more, it is crucial to build shielding around the source and the detector. This reduces the environmental background even more and it lowers the chance that shell electrons are excited by radiation. In general, graded shieldings are constructed, whereby the outer layer consists of lead. Further layers between detector and lead are necessary in order to absorb the X-rays which are emitted by the lead. Thereby the following rule applies: the lower the atomic number of an element is, the lower the energy of the generated X-rays is. For this reason the last layer should consists of light elements as aluminum or silicon. The second important step towards better analysis of the new sources is to increase the activity of the investigated samples. This could be done by irradiate the samples again by neutrons for a longer time and with smaller distance towards the neutron source. However, this would also increase the amount of parasitic nuclides which could cause a higher background again. This is especially important for the terbium source, because this source contains the isotopes ^{158}Tb and ^{160}Tb after the neutron irradiation. After the acitvation of that sample, the activity of ^{160}Tb is about as high the activity of the isotope ^{158}Tb. However, the parasitic nuclide ^{160}Tb has a lower half-life than ^{158}Tb, which means that after one year the activity of ^{160}Tb is less than 5 % of the activity of ^{158}Tb.

To conclude this, the first steps have been taken to establish a low background detector sensitive to low photon energies. Nevertheless, additional investigations are necessary to further optimize the detector setup as well as measurements with the new samples.

6 Bibliography

[1] David Attwood, Eric Gullikson, Malcolm Howells, Kwang-Je Kim, Janos Kirz, Jeffrey Kortright, Ingolf Lindau, Yanwei Liu, Piero Pianetta, Arthur Robinson, James Scofield, James Underwood, Gwyn Williams, and Herman Winick. *X-ray Data Booklet*. Lawrence Berkeley National Laboratory, University of California, Berkeley, CA, 2009 October 2009.

[2] K. Debertin and W. Pessara. Natural line-width effects in gamma- and x-ray emission rate measurements with semiconductor detectors. *Nuclear Instruments and Methods*, 184(2):497–503, 1981.

[3] K. Derbertin and R.G. Helmer. *Gamma- and X-ray spectrometry with semiconductor detectors*.

[4] IAEA. Live chart of nuclides.

[5] A. Klix, T. Döring, A. Domula, and K. Zuber. The intensive DT neutron generator of TU Dresden. *European Physical Journal Web of Conferences*, 170:Article No. 02004, 2018.

[6] Glenn F. Knoll. *Radiation Detection and Measurement*. Wiley, ISBN 978-0-470-13148-0, 4 edition, 2010.

[7] M. O. Krause and J. H. Oliver. Natural widths of atomic k and l levels, k xray lines and several kll auger lines. *Journal of Physical and Chemical Reference Data*, 8(2):329–338, 1979.

[8] Peter Lechner, Stefan Eckbauer, Robert Hartmann, Susanne Krisch, Dieter Hauff, Rainer Richter, Heike Soltau, Lothar Strüder, Carlo Fiorini, Emilio Gatti, Antonio Longoni, and Marco Sampietro. Silicon drift detectors for high resolution room temperature x-ray spectroscopy. *Nuclear Instruments and Methods in Physics Research Section A: Accelerators, Spectrometers, Detectors and Associated Equipment*, 377(2):346–351, 1996. Proceedings of the Seventh European Symposium on Semiconductor.

[9] F. Ludwig, L. Wagner, T. Al-Abdullah, G. G. Barnaföldi, D. Bemmerer, D. Degering, G. Surányi, and K. Zuber. The muon flux in the felsenkeller shallow underground laboratory. *Astroparticle Physics*, 112:24–34, 2019.

[10] Silvio Orsi. Polar: A gamma-ray burst polarimeter in space. In *2012 IEEE Nuclear Science Symposium and Medical Imaging Conference Record (NSS/MIC)*, pages 1880–1884, 2012.

[11] B. Povh, K. Rith, C. Scholz, F. Zetsche, and W. Rodejohann. *Teilchen und Kerne: Eine Einführung in die physikalischen Konzepte.* Springer-Lehrbuch. Springer Berlin Heidelberg, 2013.

[12] RaySpec. Siriussd® 170mm silicon drift detector model 881-1224a operating manual.

[13] S.I. Salem and P.L. Lee. Experimental widths of k and l x-ray lines. *Atomic Data and Nuclear Data Tables*, 18(3):233–241, 1976.

[14] T. Szücs, D. Bemmerer, D. Degering, A. Domula, M. Grieger, F. Ludwig, K. Schmidt, J. Steckling, S. Turkat, and K. Zuber. Background in -ray detectors and carbon beam tests in the Felsenkeller shallow-underground accelerator laboratory. *European Physical Journal A*, 55(10):Article No. 174, 2019.

[15] Simon Vallières. *Dose Enhancement with Nanoparticles in Radiotherapy Using Gold-Doxorubicin Conjugates.* PhD thesis, 12 2016.

A Appendix

A.1 Baseline of SDD
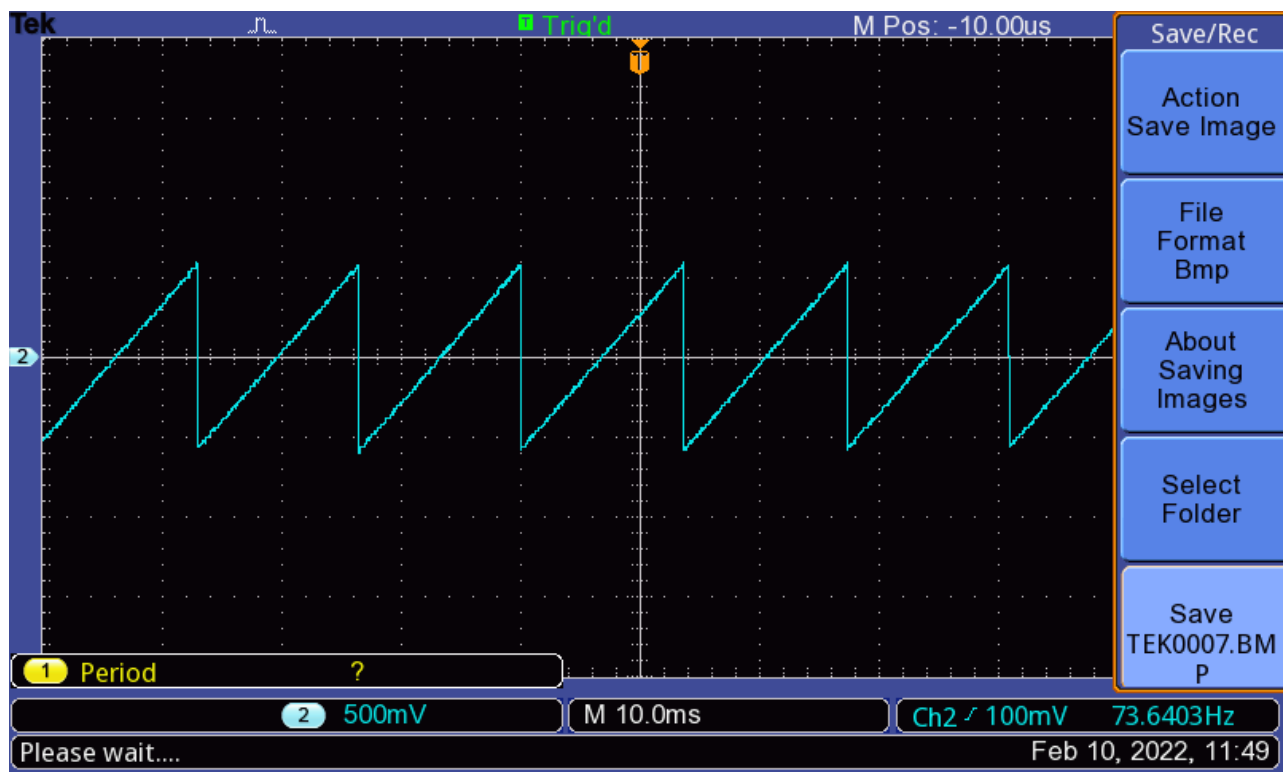
Figure A.1: Sawtooth-like baseline of a silicon drift detector due to leakage current and rest pulse.

A.2 Digitizer settings in "CoMPASS"-Software

Parameter	Board	CH0	CH1	CH2	CH3	CH4
Enable	☐	☑	☐	☑	☐	☑
Record length	20000 ns					
Pre-trigger	2000 ns	2000 ns	2000 ns	2000 ns	2000 ns	2000 ns
Polarity	Positive	Positive	Positive	Negative	Positive	Negative
N samples baseline	256 samples	1024 samples	256 samples	4096 samples	256 samples	4096 samples
DC Offset	20.0 %	5.0 %	20.0 %	6.0 %	20.0 %	6.0 %
Coarse gain	1x	4x	1x	1x	1x	1x

Figure A.2: "Input"-settings within the "CoMPASS"-software (PHA firmware).

Parameter	Board	CH0	CH1	CH2	CH3	CH4
Threshold	100 lsb	20 lsb	100 lsb	130 lsb	100 lsb	130 lsb
Trigger holdoff	480 ns	480 ns	480 ns	288 ns	480 ns	288 ns
Fast Discriminator smoothing	4 samples	64 samples	4 samples	4 samples	4 samples	4 samples
Input rise time	96 ns	96 ns	96 ns	48 ns	96 ns	48 ns

Figure A.3: "Discriminator"-settings within the "CoMPASS"-software (PHA firmware).

Parameter	Board	CH0	CH1	CH2	CH3	CH4
Trap. rise time	4.992 µs	4.992 µs	4.992 µs	2.000 µs	4.992 µs	2.000 µs
Trap. flat top	0.992 µs	2.000 µs	0.992 µs	0.992 µs	0.992 µs	0.992 µs
Trap. pole zero	50.000 µs	100.000 µs	50.000 µs	0.176 µs	50.000 µs	0.176 µs
Peaking time	80.6 %	31.2 %	80.6 %	45.2 %	80.6 %	45.2 %
N samples peak	1 sample	64 samples	1 sample	16 samples	1 sample	16 samples
Peak holdoff	0.992 µs	0.992 µs	0.992 µs	0.992 µs	0.992 µs	0.992 µs
Energy fine gain	1.000	1.240	1.000	1.500	1.000	1.500

Figure A.4: "Trapezoid"-settings within the "CoMPASS"-software (PHA firmware).
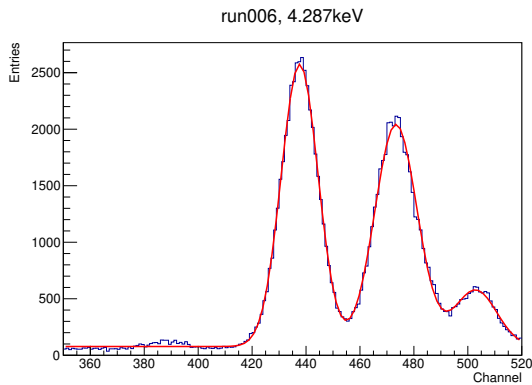
A.3 Full length of ^{133}Ba and ^{57}Co
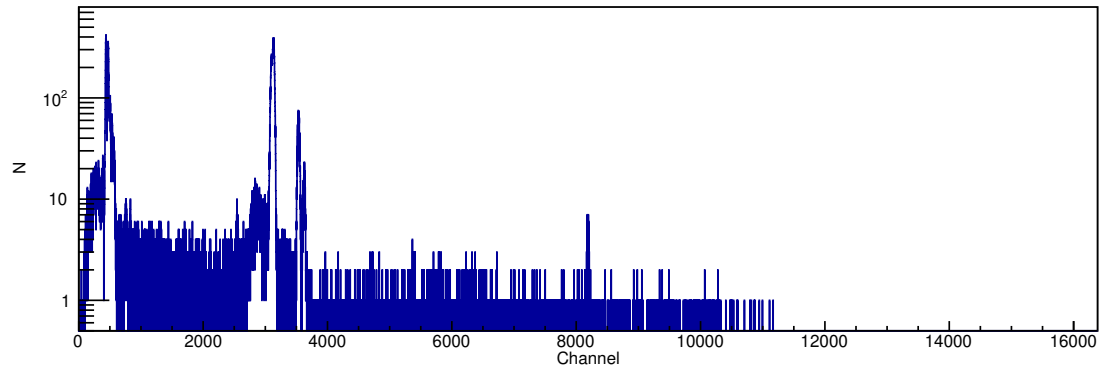
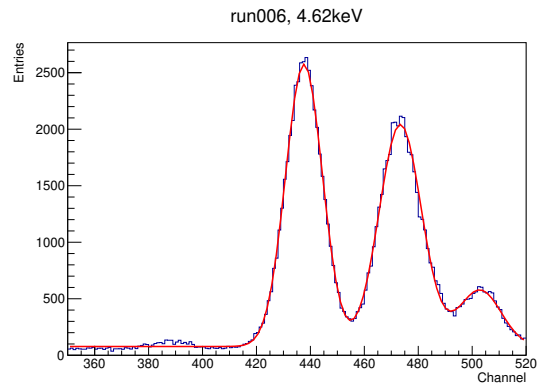**Figure A.5:** Spectrum of ^{133}Ba shown in figure 4.1 over the full range of channels.
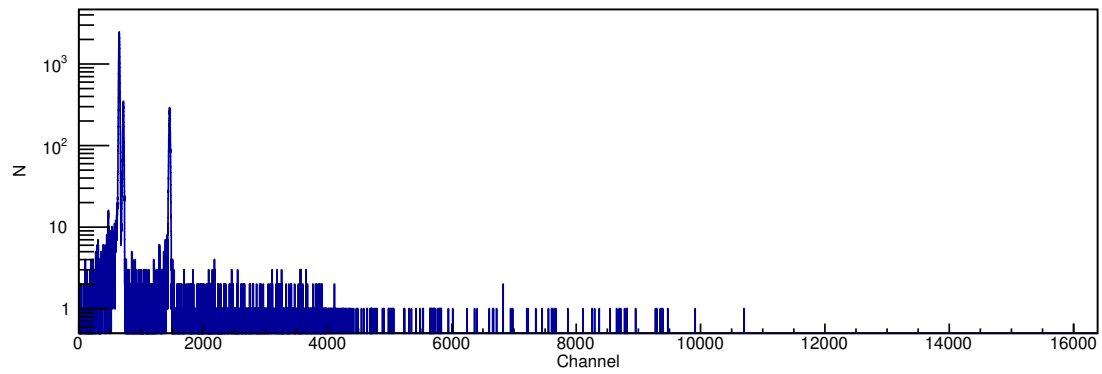
Figure A.6: Spectrum of ^{57}Co shown in figure 4.2 over the full range of channels.

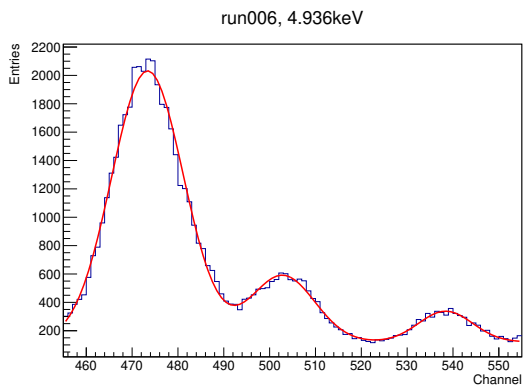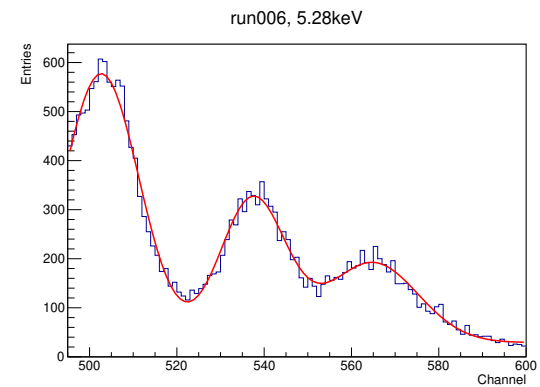# A.4 Fitted detector calibration peaks

run006, 4.287keV

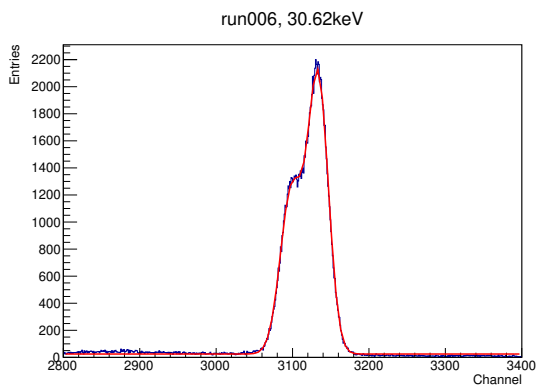**Figure A.7:** Lα_1-line of ^{133}Ba

run006, 4.62keV

Figure A.8: Lβ_1-line of ^{133}Ba.

run006, 4.936keV

Figure A.9: Lβ_2-line of ^{133}Ba.

run006, 5.28keV

Figure A.10: Lγ_1-line of ^{133}Ba.

run006, 30.62keV
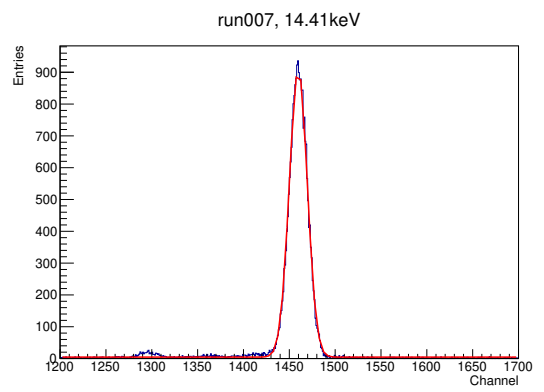
Figure A.11: Kα_2-line of ^{133}Ba.

run006, 30.97keV
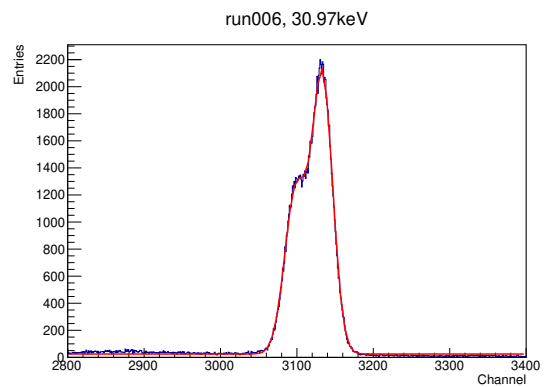
Figure A.12: Kα_1-line of ^{133}Ba.
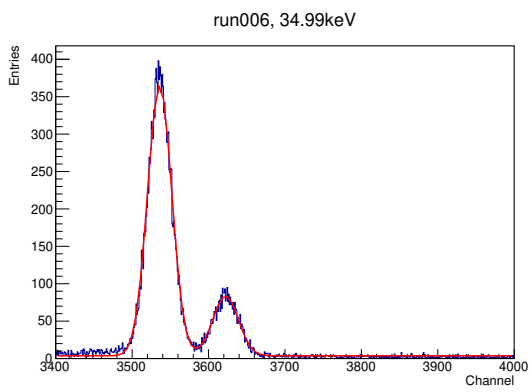
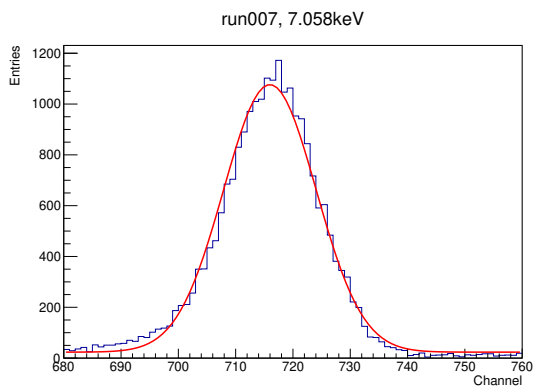**Figure A.13:** Kβ_1-line of ^{133}Ba.

Figure A.14: Kβ_1-line of ^{57}Co.

Figure A.15: γ-ray line of ^{57}Co.

Danksagung

Zuerst möchte ich meinen Betreuern Hans F. R. Hoffmann, Marie Pichotta und Steffen Turkat ganz besonders danken. Sie haben mich während der gesamten Arbeitszeit in jeder Hinsicht unterstützt und mir das wissenschaftliche Arbeiten näher gebracht.

Ich möchte mich außerdem recht herzlich bei Prof. Kai Zuber bedanken, dass ich diese Arbeit als Teil seiner Arbeitsgruppe schreiben durfte. Ich danke auch den übrigen Mitgliedern der Arbeitsgruppe, die mich ebenso mit einigen Hinweisen während der Arbeitszeit unterstützt haben.

Erklärung

Hiermit erkläre ich, dass ich diese Arbeit im Rahmen der Betreuung am Institut für Kern- und Teilchenphysik ohne unzulässige Hilfe Dritter verfasst und alle Quellen als solche gekennzeichnet habe.

Christoph Seibt
Dresden, Februar 2022